Evidence for a Current System and Potential Structure in the Martian Magnetotail

Murti Nauth[1,2], David L. Mitchell[1], Christopher M. Fowler[3], and Imke de Pater[2,4]

[1]Space Sciences Laboratory, University of California, Berkeley, California, USA
[2]Department of Earth and Planetary Science, University of California, Berkeley, Berkeley, CA, USA
[3]Physics and Astronomy, West Virginia University, Morgantown, WV, USA
[4]Department of Astronomy, University of California, Berkeley, Berkeley, CA, USA

Key Points:

- The Martian magnetotail exhibits complex morphology and topology downstream of strong crustal magnetic field sources.
- Multiple magnetic field rotations on spatial scales that are small compared to the overall magnetotail dimensions reveal currents, suggesting the presence of multiple current regions.
- Counter-streaming electrons, which are rare in the magnetotail, are twice as likely to occur downstream of strong crustal magnetic fields when they are located near the evening terminator.

Corresponding author: Murti Nauth, murtinauth@berkeley.edu

Abstract

We present a case study of plasma and magnetic field observations in the Martian magnetotail using data from the Mars Atmosphere and Volatile EvolutioN (MAVEN) mission during an orbit when the spacecraft was in the optical shadow, past the dusk terminator and downstream of the strongest crustal magnetic fields. In this region, we observed multiple magnetic field rotations and amplitude drops (signatures of currents) closely associated with energized (up to 100 eV) electron populations. Several transitions between closed and draped magnetic topologies also occur in this region, which are likely to be caused by magnetic reconnection between the IMF and crustal magnetic fields. We also observe two regions of energized, counter-streaming electrons, which are rare in the magnetotail, but twice as likely to occur downstream of strong crustal magnetic fields when they are near the evening terminator. Together, the multiple magnetic field rotations, topological changes, and counter streaming electrons suggest the presence of an electric potential structure similar to those observed above the auroral arc regions at Earth.

Plain Language Summary

Mars does not have a global dipole magnetic field, but a fraction of the planet's crust carries strong remanent magnetization, which affects the plasma environment. When the magnetized solar wind encounters Mars, its magnetic field drapes around the conducting ionosphere and crustal magnetic fields and forms a magnetotail downstream of the planet. Reconnection between the solar wind magnetic field and crustal magnetic fields occurs often, resulting in a complex and changing configuration of open, closed, and draped magnetic field lines. Reconnection and reconfiguration of the magnetic field releases stored energy and drives currents, which energize the plasma. The energized plasma can precipitate onto the atmosphere and cause aurora. In this paper, we present a case study of plasma and magnetic field observations when the MAVEN spacecraft was downstream of strong crustal magnetic fields located near the evening terminator. Multiple magnetic field rotations, topological changes, and energized plasma indicate that reconnection gives rise to a complex magnetic environment downstream of the crustal fields. We found counter-streaming electrons in the magnetotail, an observation which is thought to be a signature of the potential structure that energizes the auroral electrons, and are commonly observed at high altitudes above auroral regions at Earth. Therefore, we consider the observations in this study to be possible precursors to discrete auroral activity in Mars' crustal magnetic field regions.

1 Introduction

Mars lacks a global dipole magnetic field, but the interaction of the magnetized solar wind with the conducting ionosphere induces a magnetosphere around the planet. The presence of thermal remanent crustal magnetic fields (Acuña et al., 1998) affect the Martian plasma environment and effectively create a hybrid magnetosphere. In the regions where the strongest crustal magnetic fields are located, the crustal fields themselves standoff the solar wind up to 1000km in altitude. This standoff distance is well above the ionosphere, which means that in these regions, non-uniform "mini-magnetospheres" can exist. A commonality between induced and intrinsic magnetic fields include the flared "tail" produced behind the planet (Vaisberg & Smirnov, 1986) by the interplanetary magnetic field (IMF) draping about Mars. Because of the lack of an intrinsic global magnetic field, the magnetotail of Mars is similar to what is observed in fully unmagnetized bodies with ionospheres (e.g. Venus, Titan). Within the magnetotail region are two magnetic field lobes that are oriented in opposite directions and are separated by a central current sheet.

The complex interaction between the IMF and localized crustal magnetic fields that rotate with the planet leads to dynamic plasma processes throughout the induced mag-

netosphere, including the magnetotail region, which is the focus of this study. Early explorers, like the Phobos spacecraft, discovered that orientation and polarity of the two-lobe magnetotail structure varied depending on the upstream solar wind orientation (Yeroshenko et al., 1990). Later explorers, like Mars Global Surveyor (MGS), Mars Express, and the Mars Atmosphere and Volatile EvolutioN (MAVEN) mission have shown convincing evidence that the magnetic field reconnects and reconfigures in the tail region (DiBraccio et al., 2015; Eastwood et al., 2012; Halekas et al., 2009; Harada et al., 2015). When the crustal magnetic fields reconnect with the IMF, closed loops can open into the tail region (Luhmann et al., 2015; Weber et al., 2020). The entire Martian magnetosphere (bow-shock and near-tail magnetosheath) can respond to changes in the upstream IMF conditions on timescales as short as 10 minutes (Romanelli et al., 2018).

Reconnection between the IMF and crustal fields can lead to a variety of magnetic field topologies in three basic categories: open, closed, and draped. Topology refers to the large-scale connectivity of magnetic field lines. IMF lines are usually connected to the solar atmosphere on one or both ends, but they occasionally disconnect from the Sun (Gosling et al., 2005). These field lines are carried by the solar wind, and can drape over the Mars obstacle while maintaining this topology. Near the planet, the IMF can reconnect with planetary crustal fields to alter the topology, so that one end of the line intersects the planetary atmosphere at a "foot point"—the altitude at which electrons are absorbed via collisions with the neutral atmosphere. Closed crustal magnetic loops have two such foot points. The properties of electrons that are constrained to follow these field lines provide information about the source regions sampled by the field line at large distances from the measurement location, as well as acceleration processes (e.g. electric fields) that they encounter. Our study deduces topology from electron energy and pitch angle distributions (PADs) using the methods from Xu, Weber, et al. (2019); D. Brain et al. (2007); Weber et al. (2017). Mapping topology in the magnetotail allows us to understand how energy and momentum are exchanged between the solar wind and the planet, how solar wind particles penetrate onto the ionosphere, and how electrons become accelerated.

Crustal magnetic fields play an important role in driving plasma processes and magnetic field morphology, resulting in complex signatures in the magnetotail region. They are thought to be responsible for a variable ($<45°$) twist in the inner magnetotail lobes and current sheet, depending on the upstream IMF direction (DiBraccio et al., 2018). The location of the strongest crustal fields have also been shown to affect the distribution of thermal electrons in the magnetotail region (Nauth et al., 2021) as well as the occurrence of discrete aurora (Schneider et al., 2021). Much of these magnetotail observations suggest a strong relationship between the crustal fields and observed magnetotail structure. Such dynamics are important for understanding the Martian magnetospheric structure, the interaction between the solar wind and Mars, and the processes which maintain the nightside ionosphere.

Since its arrival at the red planet, the MAVEN mission (Jakosky et al., 2015) has been providing in-situ particle and field observations throughout the Mars environment, including the magnetotail region. MAVEN observed a variety of processes in the magnetotail region that include magnetic reconnection (Harada et al., 2015), current sheet crossings and associated tailward flow of high energy planetary ions (DiBraccio et al., 2015), and detached magnetic flux ropes (Hara et al., 2017).

In this work, we present a time sequence of MAVEN plasma and magnetic field data obtained while the spacecraft was in the magnetotail near the evening terminator, downstream of the strongest crustal fields. We focus on 30 eV-1keV electrons, whose small gyro-radii and short gyro-periods confine their gyration about the magnetic field and allow us to probe their source regions and acceleration mechanisms. Identifying the source regions of electrons traveling parallel and anti-parallel to the magnetic field allows us to infer the topology and large-scale configuration of the magnetic field.

The coordinate system used in this study is the Mars Solar Orbital (MSO) system, where the X axis points from Mars to the Sun, the Z axis points toward Mars' ecliptic north, and the Y-axis completes the right-handed coordinate system.

In section 2, we describe the instruments used in the study. Section 3 provides an overview of the observations. Section 4 describes our results. Finally, we discuss our results in section 5 and summarize conclusions in section 6.

2 Instruments

This study uses data from the MAVEN spacecraft's particles and fields package: the Solar Wind Electron Analyzer (SWEA) (Mitchell et al., 2016), Magnetometer (MAG) (Connerney et al., 2015), and SupraThermal And Thermal Ion Composition (STATIC) (McFadden et al., 2015). SWEA is an electrostatic top-hat analyzer with deflectors that is mounted on the end of a 1.5-meter boom on the spacecraft. It measures electron fluxes (within 3eV-5keV energy range) at a cadence of 2-4 seconds, with an energy resolution ($\Delta E/E$) of 17%. For energies <2keV, SWEA's field of view (FOV) during each sweep is 360° × 120°, which allows the instrument to observe 87% of the sky (Mitchell et al., 2016). Given the instrument's location relative to the spacecraft, MAVEN blocks 8% of SWEA's FOV. MAG includes two tri-axial fluxgate magnetometers which measure the local magnetic field vector from about 0.1 nT up to 3000 nT with a sampling rate of 32 Hz (Connerney et al., 2015). Note that the MAG data are averaged over 1 s for this study. A combination of magnetic field vector and SWEA electron distributions can be used to obtain suprathermal electron energy-pitch angle distributions that are available from the Planetary Data System (PDS). SWEA's wide field of view usually provides complete pitch angle coverage (0-180 degrees), although the instrument's blind spots and spacecraft blockage sometimes reduce this coverage. STATIC is a toriodal electrostatic analyzer which measures ions as a function of energy (0.1 eV - 30 keV) and direction (22.5° resolution orthogonal to the deflection plane and variable resolution in the deflection plane). Time-of-flight mass measurements allows STATIC to resolve major ion species in the Martian ionosphere, as well as planetary and solar wind ions at higher altitudes.

3 Observations

The data for this study were obtained during 2017-12-11/08:30-09:20 UTC. For this orbit, MAVEN's periapsis is located on the dayside (Figure 1, plus symbol: solar zenith angle = 65 deg, latitude = -21.7 deg, local time = 8.8 h), and the inbound portion of the orbit (apoapsis to periapsis, light to dark green) samples the magnetotail region (Figure 1, panels a and b). The strongest crustal magnetic fields are straddling the evening terminator, and the spacecraft is downstream of these fields. MAVEN particle and fields observations from 08:30 (marked on the orbit in Figure 1) to 09:30 are shown in Figure 2.

After the spacecraft enters the optical shadow (Figure 2 line A), the particles and magnetic field measurements exhibit typical magnetotail signatures. The observed magnetic field is nearly in the MSO XY plane, (elevation ∼-13 deg), and flares away from the X axis (azimuth ∼340 deg), as shown in Figure 2, panels h and g, respectively. The electron distributions also have the shape of a quiescent tail lobe population, such as what is shown in Figure 3. The electron energy spectrum exhibits a low and slowly decreasing energy flux from 10 to 200 eV and falls more steeply at higher energies. These signatures are consistent with solar wind electrons decelerated by the tail potential (Xu, Poppe, et al., 2019; Mitchell et al., 2016). Note that the dashed black line in Figure 2 panel a is the nominal dividing line between secondary and ambient electrons for the energized electron spectra, as described in section 3 of Mitchell et al. (2016). Finally, the ions have very low energies, with O^+ and O_2^+ at 14 eV, and light ions at a few eV in the plasma frame (corrected for a -8 V spacecraft potential, and spacecraft velocity).

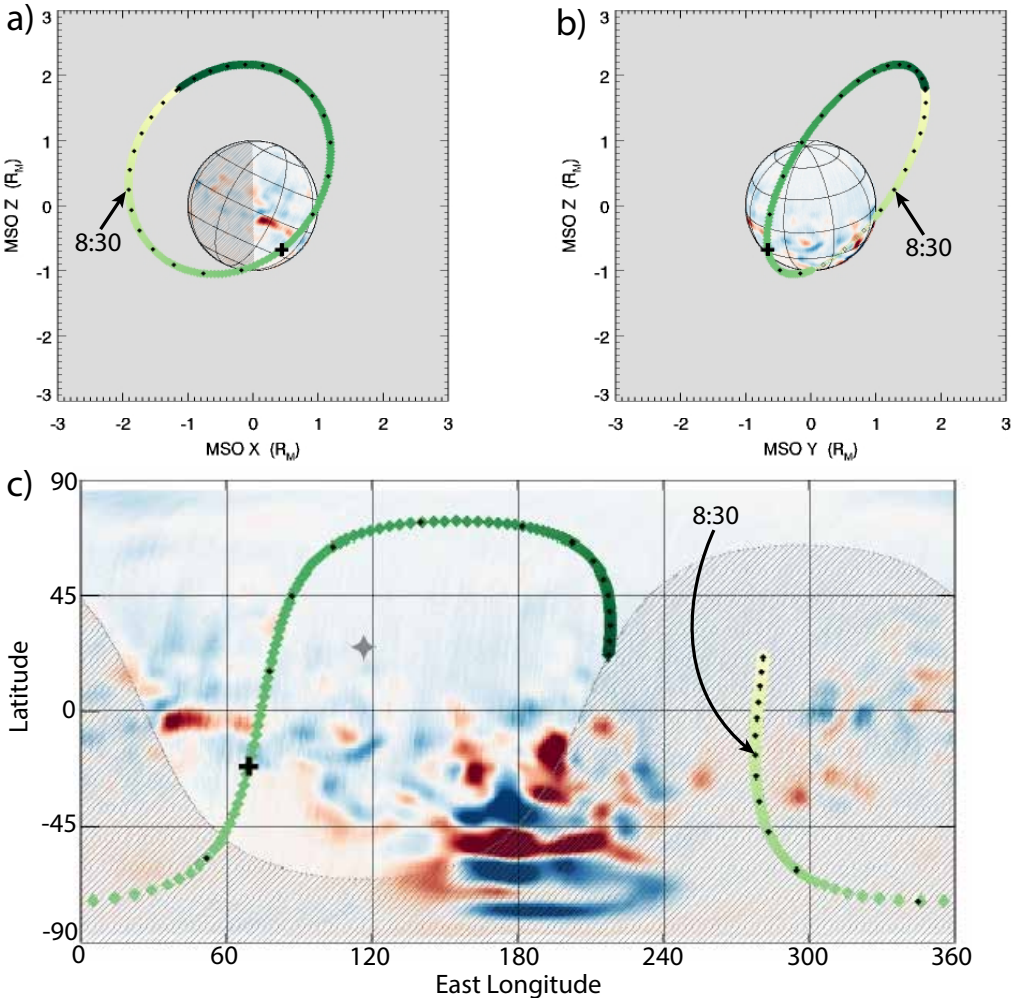

Figure 1. MAVEN's orbit about Mars during the case study. Panel a (b) show MSO XZ (YZ) projections, and panel c shows a rectangular projection of Mars showing average crustal field strengths at 400km from MGS. The orbit's color gradient becomes darker as time progresses, the black dots mark 10 minute intervals, and periapsis is the plus symbol. Note that the spacecraft trajectory is downstream of strong crustal magnetic sources located near the evening terminator.

At 08:43 UTC, the spacecraft enters a region with markedly different plasma conditions, and over the course of the next 18 minutes, the magnetic field exhibits multiple large rotations and associated drops in amplitude, which indicate the presence of currents. Electron acceleration, as inferred from shifts in the peak energy flux to higher energies (e.g. Figure 3), is also observed close in time with the field rotations. Two electron spectra from this time of acceleration are compared to the quiescent tail lobe in Figure 3, showing clear peaks in the accelerated populations compared to a quiescent tail population.

The magnetic field rotations are more clearly seen in Figure 4, which shows the XZ (panel a) and XY (panel b) projection of the observed magnetic field directions, normalized to unit length. The gray directions are the instances when the spacecraft is outside the optical shadow and region of interest. The colored directions show the times when

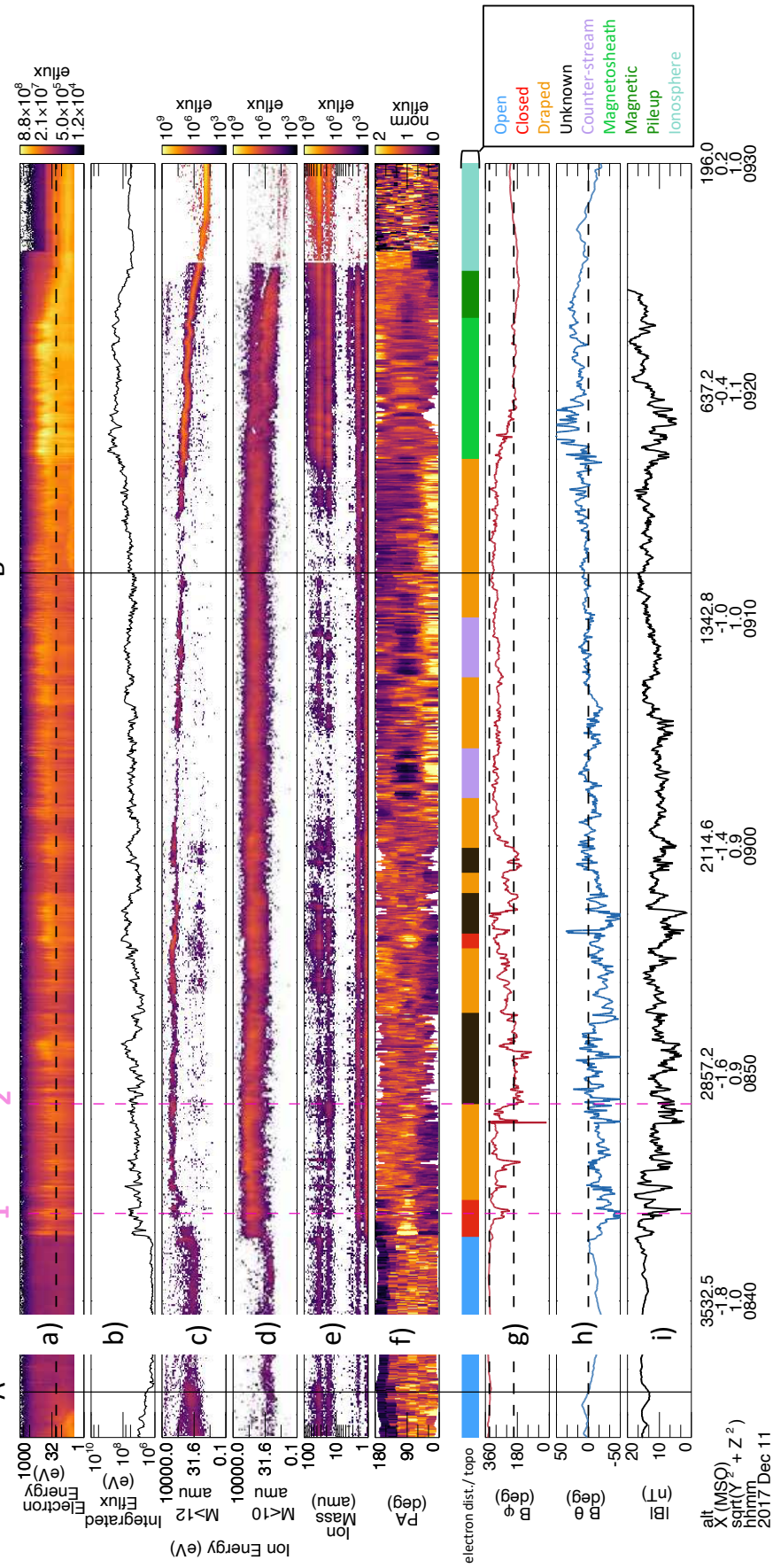

Figure 2. Times series of MAVEN particles and fields data spanning the events for this study. From top to bottom: electron energy spectra (panel a), with the colorscale showing differential energy flux (eV cm^{-2} s^{-1} ster^{-1}eV^{-1}), the dashed horizontal black line represents the nominal dividing line between secondary and ambient electrons for the energized electron spectra (see section 3 of Mitchell et al. (2016)); electron energy flux, integrated over 30-1000 eV (panel b); Energy flux of heavy ions (M > 12 amu) and light ions (M < 10 amu) as a function of energy and time (panels c and d, respectively); Ion energy flux as a function of mass and time (panel e); Normalized 111-140-eV electron energy flux as a function of pitch angle and time —the data are normalized to unity at each time step to remove the overall variation with time and emphasize the pitch angle distribution (panel f); a colorful bar of deduced topologies and electron distributions (see inset for legend); Magnetic field azimuthal component (φ, panel g), elevation (θ, panel h), and amplitude (panel i) in units of degrees and nT, respectively. The dashed horizontal lines in panel g correspond to east (360 deg) and west (180 deg) magnetic field azimuth and the dashed horizontal line in panel h corresponds to a horizontal (0 deg) magnetic field elevation (in the MSO frame).

The solid black lines (A, B) mark the times the spacecraft enters (A) and exits (B) the optical shadow, and the analysis in this paper focuses on the data collected between lines A and B. The dashed magenta lines (1, 2) are two times among many when the spacecraft crosses a current region.

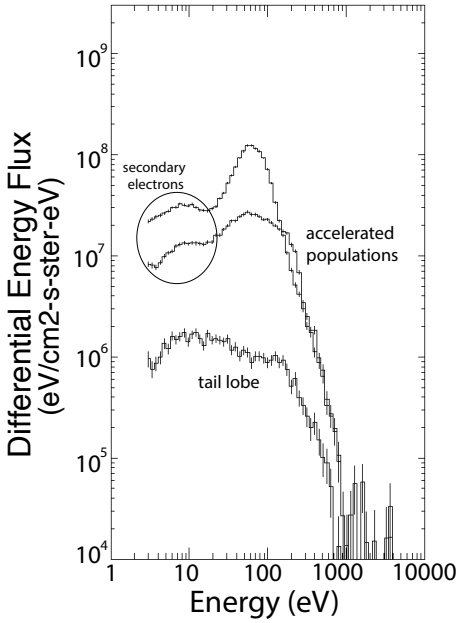

Figure 3. Electron energy distributions for a quiescent tail lobe (08:43) and two times (08:55, 09:08) of energization. Note the secondary electron contamination at lower energies of the accelerated population create an artificial enhancement of energy flux. The sharp peaks in the electron distributions are characteristic of energization.

the spacecraft is within the optical shadow, with each color representing the peak energy of the electron energy flux, summed over 4 seconds. If a peak in the electron energy flux is identified within 30-1000 eV, then the energy at which the peak flux is identified is recorded. If no peak was identified because there was insufficient energization, then a color value of 30 eV was assigned to that line. In figure 4, points A and B correspond to the solid black lines A and B in Figure 2, marking the time when the spacecraft enters and exits the optical shadow.

Ions are also accelerated over the region of study. Light and heavy ion energy distributions become broader and shift to higher energy, as shown in Figure 5. Panels a and b show energy fluxes for heavy ions (O^+ and O_2^+) and light ions (H^+ and H_2^+), velocity moments for H^+, O^+, and O_2^+ (panels c-e), and energy vs mass spectra at times indicated by the green shaded regions (panels 1-4). Moving backwards in time (from right to left on the time series in Figure 5), planetary H^+ becomes much hotter and travels tailward at 230 km/s (panel c) and planetary O^+ and O_2^+ are traveling tailward at 100 km/s (panels d and e), having been accelerated up to 1 keV. Note that between shaded boxes 1 and 3, O^+ and O_2^+ are traveling at the same energy (panel a) with velocities that differ by about the square root of the mass ratio (panels d-e). Energization up to 1 keV in the tail indicates that the ions are likely being accelerated by the $\mathbf{j}\times\mathbf{B}$ force. Light ions reach energies from tens of eV up to 1 keV. This broader range of acceleration is likely caused by the more extended distribution of hydrogen around the planet, as compared to the heavy ions. Consequently, light ions experience a broader range of total acceleration.

Regarding the origin of each ion species, the O^+ and O_2^+ are of planetary origin, and the light ions with a mass/charge of 1 and 2 are ambiguous: they could be solar wind

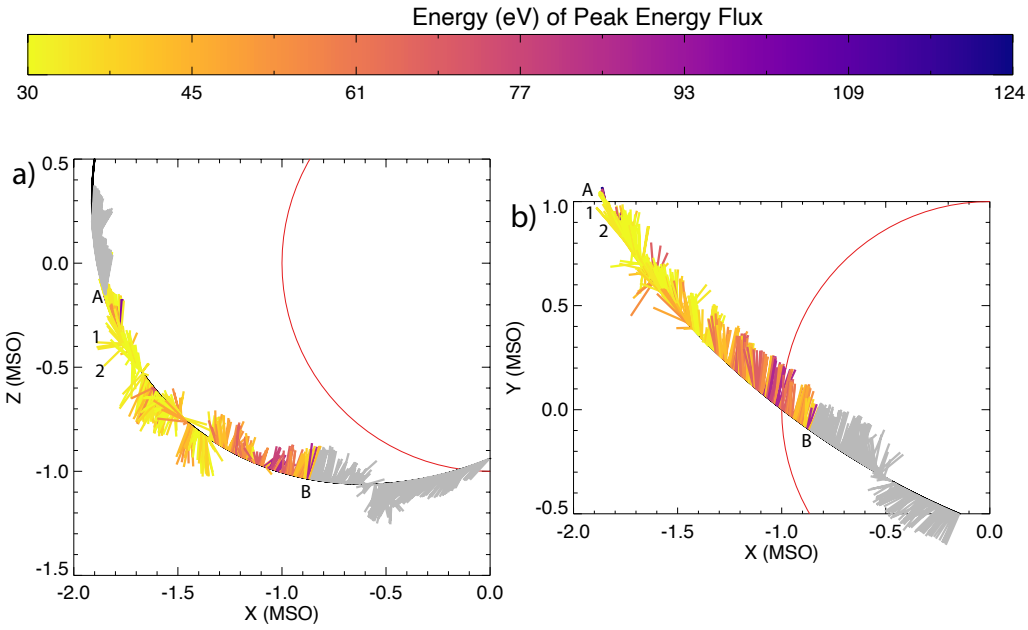

Figure 4. Magnetic field direction along the MAVEN orbit trajectory projected on the MSO XZ (a) and XY (b) planes, with axes in units of Mars radii (1 R_M = 3389 km). All vectors have unit length to emphasize the magnetic field rotations. Colored (gray) vectors are inside (outside) the optical shadow. The color scale encodes the peak energy of the electron energy flux spectrum at the time of each magnetic field measurement. Darker colors (higher peak energies) show times of electron energization. Labels correspond with timestamps of the lines in Figure 2.

H^+ and He^{++} or planetary H^+ and H_2^+. This ambiguity is resolved by the presence of a "ghost peak" at m/q = 11.4 (blue lines in Figure 5 panels 1-4), which is an instrumental effect caused by dissociation of H_2^+ at the start foil of the time-of-flight detector (see McFadden et al. (2015)). The presence and intensity of the ghost peak shows that the peak at m/q = 2 is dominated by H_2^+. Thus, the light ions are also of planetary origin.

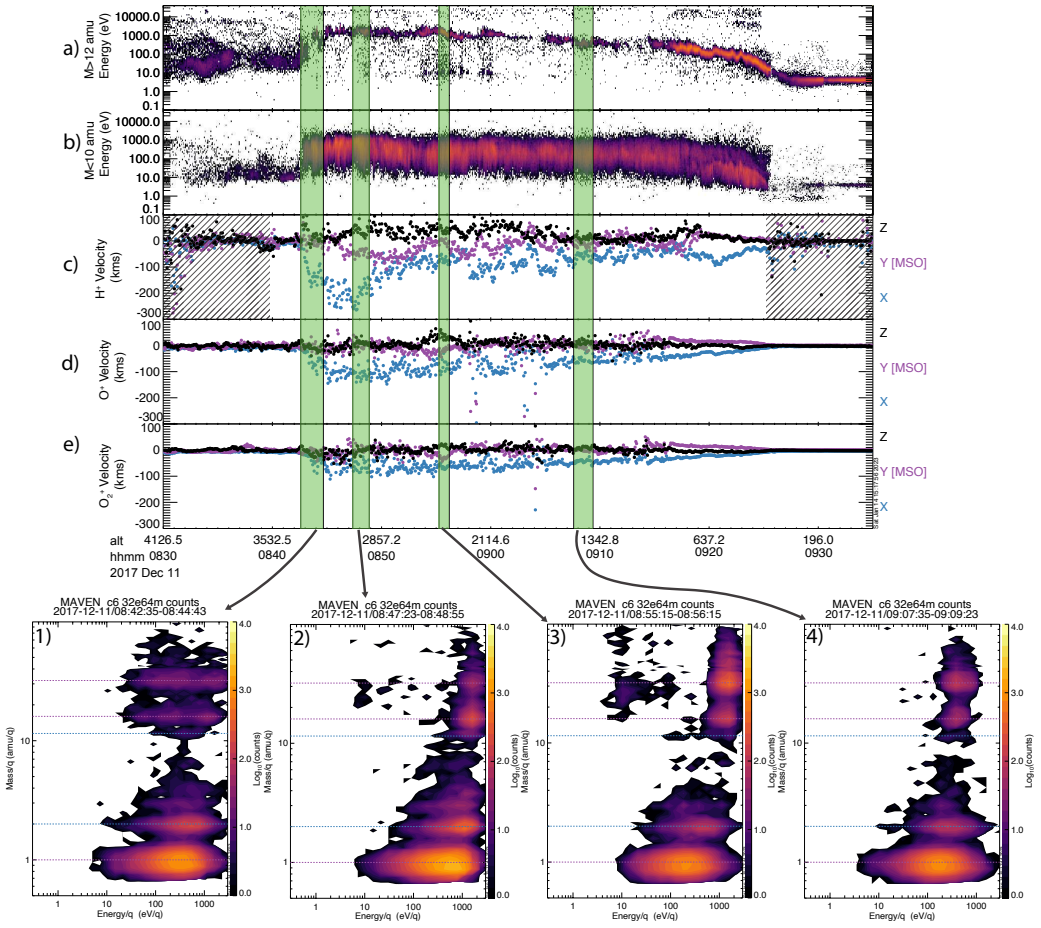

Figure 5. Panels a and b show the time series of energy flux of heavy ions (M > 12 amu) and light ions (M < 10 amu). H^+, O^+ and O_2^+ velocities in the MSO frame (panels c, d, and e, respectively) are shown. These velocities were calculated by taking moments of the measured ion distribution functions, as functions of velocity (energy) and look direction, using the standard moment integrals. Low count rates are covered in the hatched pattern in panel c and are not included in the analysis. The numbered inserts show ion energy/charge versus mass/charge for 4 selected time intervals, marked by the green shaded regions covering the time series data. Each horizontal line in panels 1-4 highlight masses at 1 (H^+), 2 (H_2^+), 11.4 (ghost peak), 16 (O^+), and 32 (O_2^+) amu.

4 Results

4.1 Topological Changes

Using electron pitch angle and energy distributions, we deduced the magnetic field topology and show each region in the electron dist/ bar in Figure 2, titled "electron dist./ topo." This panel shows the averaged electron distributions and magnetic field topology over time and space. Initially, an open topology is inferred based on the presence of a one-sided loss cone (150-180 deg), which is partially filled (15%) by backscattered electrons (Figure 2f). Either the magnetic field extends down to the planet's surface and is connected to a crustal source, or it is a "deeply draped" IMF field line, with part of the line descending below the electron exobase. This open topology is blue in the electron dist./ topo bar in Figure 2.

After the rotations in the magnetic field begin, the topology is predominantly draped (orange in Figure 2. electron dist./ topo bar), interrupted by brief intervals of unknown (black) and closed (red) topology. The unknown topology was due to the lack of complete pitch-angle coverage. The closed topology means that the electrons are trapped onto the magnetic field, and the field rotates by 65 degrees and 45 degrees during each respective period of trapping. We show normalized electron energy fluxes and pitch angle resolved energy spectra for a 1-minute observation of trapping in Figure 6 (panels a-c). The electron flux is enhanced at pitch angles around 90 degrees (Figure 6 panels a and b), and electron pitch angles range from ∼60 deg. to ∼120 deg. Correspondingly, the pitch angle resolved energy spectra (Figure 6 panel c) shows greater flux at energies above 30 eV for the 90 deg. population (green line) compared to the field aligned directions (red and blue lines). The perpendicular population peaks at a higher energy (60eV), compared to the parallel population, indicating a temperature anisotropy. Note that the broad, featureless energy distribution (panel c) indicates that the electrons are of solar wind origin. Panels a-c in Figure 6 show one example of trapping; this topology is observed several times throughout the portion of the orbit analyzed in this study.

The majority of magnetic field topology during this orbit segment was draped; however, there are two regions that show beamed electrons in both field-aligned directions, where we cannot infer magnetic topology using the methods of Xu, Weber, et al. (2019). These populations are considered "counter-streaming" and correspond to the purple portions of the electron dist/topo bar in Figure 2. We selected one instance of counter-streaming and show the electron energy fluxes and pitch angle resolved energy spectra in Figure 6 panels d-f. The electron flux is enhanced at pitch angles above 120 degrees and below 60 degrees (Figure 6 panels d and e). Although, the parallel and anti-parallel beams have different fluxes, with the anti-parallel beam peaking at a slightly higher energy. The pitch angle resolved energy spectra (Figure 6 panel f) shows greater flux at energies above 20 eV for the field aligned directions (red and blue lines) compared to the 90 deg. population (green line). The significance of this counter-streaming will be discussed in section 4.3 below.

4.2 Example Current Regions

There are numerous magnetic field rotations ranging from 45 to 120 degrees during a substantial portion of the time series. Most but not all of these have associated drops in the magnetic field amplitude, which is consistent with the presence of currents. The two lobes of a classical magnetotail, such as at Venus, would be separated by a single current sheet marked by a 180-degree rotation and a drop in the magnetic field amplitude. The more complex behavior of the magnetic field in our case study does not allow us to infer the geometry of the currents, so we refer to them as current regions. Figure 7 shows the electron and magnetic field data from the time series in Figure 2, but zoomed in near the dashed magenta lines (labeled 1 and 2 in Figure 2) to show finer details.

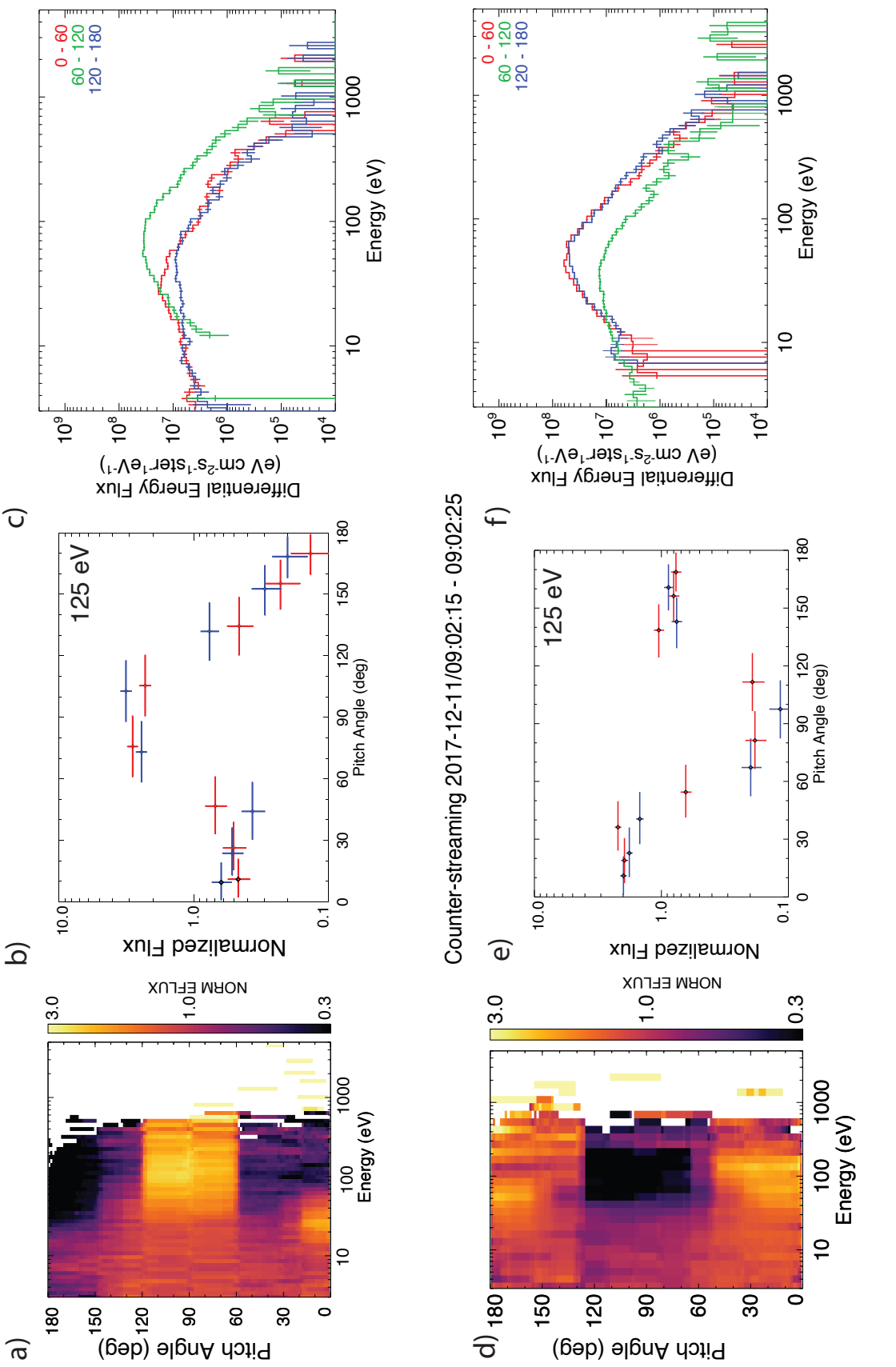

Figure 6. For a trapped (counter-streaming) population, panels a-c (d-f) show normalized flux as a function of energy and pitch angle, normalized flux as a function of pitch angle, and differential energy flux as a function of energy. In panels b, and e, horizontal bars show the range of pitch angles sampled in each bin, and sets of red and blue symbols indicate independent measurements on opposite sides of the detector. Vertical bars in panels b-c and e-f show the statistical uncertainty (one standard deviation). Secondary electron contamination is present below 20 eV and dominates below 10 eV.

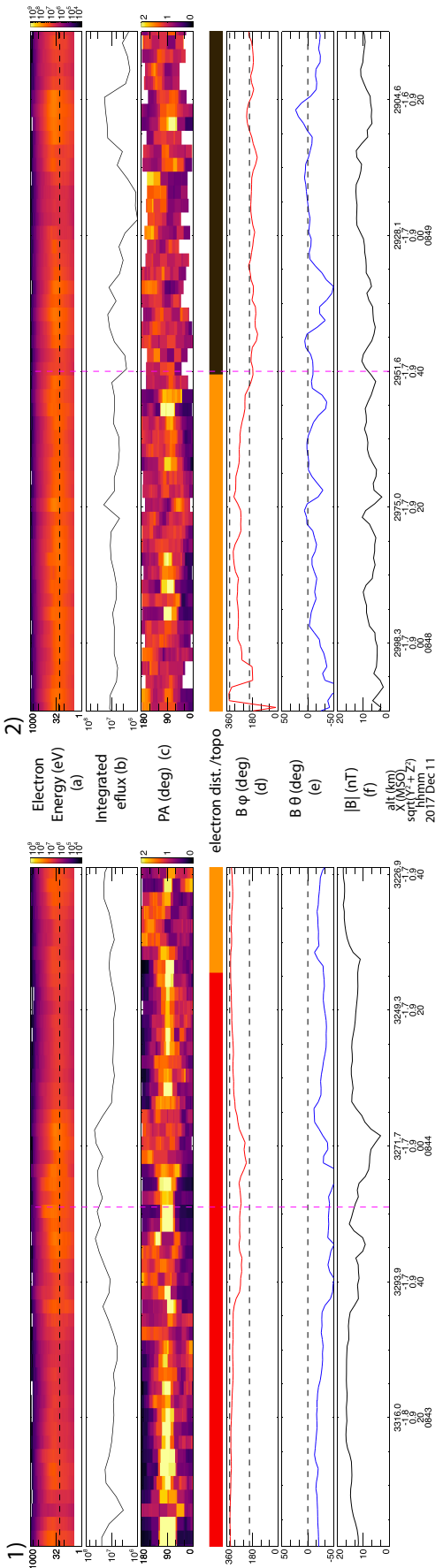

Figure 7. Zoomed in time series of the electron and magnetic field data, during the time surrounding current region crossings (dashed magenta lines). These times correspond to the vertical dashed magenta lines (1 and 2) in Figure 2. From top to bottom: electron energy flux, integrated (300-1000 eV) electron energy flux, electron pitch angle distributions averaged from 110 to 140 eV, electron distribution bar (see Figure 2 for legend), MSO azimuth (φ), elevation (θ), and amplitude.

The first example (Figure 7.1) shows electron and magnetic field data for the trapping region from 8:43 to 8:44:30. The trapped topology is interrupted during two ∼8-second intervals centered near 8:43:25 and 8:44:05. The magnetic field rotates by 45 degrees during the first interval, and then back to the original direction during the second interval. Each rotation is associated with a drop in the magnetic field amplitude, indicating the presence of currents.

In the second example (Figure 7.2), the magnetic field rotates through 112 deg. Electron energy flux enhancements are evident in panels a and b. The magnetic field has a mean amplitude of 8 nT, with several drops down to 2-5 nT. The main field rotation (8:48:22 to 8:48:45) is near two of these drops. On a larger scale, the tail lobe field strength away from this region is 15 nT (Figure 2, line A). Unlike the previous example, the magnetic field amplitude and direction remain steady at the new values after the field rotation, indicating that the spacecraft remains on the other side of the current region. In places where the magnetic field topology can be determined, the topology is draped, indicated by the orange color of the electron dist/topo bar.

4.3 Counter-streaming electrons

The presence of counter-streaming electrons in the magnetotail was surprising and motivated further investigation. To test whether the counter-streaming we observed in this case study was significant, we used the padscore database (Weber et al., 2017) to search for counter-streaming in the magnetotail between 2014 and 2021. The padscore database provides a score based on the ratio of parallel to perpendicular electron energy fluxes and assigns an "up" (away from the planet) and "down" (towards the planet) score to each timestamp (see Weber et al. (2017) for an explanation of this method).

Figure 8 shows the counting-statistics and the likelihood of observing counter-streaming within a cylinder centered on the MSO X axis with a radius of 1 Mars radius (Rm) and extending from X = -1 to -3 Rm. Statistics are obtained for four orientations of the planet with respect to the Mars-Sun line and for two halves of the cylinder, Y$>$ 0 (dusk) and Y $<$ 0 (dawn). Panel a shows the total number of pitch angle spectra obtained as a function of location within the cylinder. The duskward (Y MSO $>$ 0) and dawnward (Y MSO $<$ 0) halves are shown in panels b-e and f-i , respectively. An observation was considered counter-streaming when both the parallel and anti-parallel fluxes were greater than the perpendicular flux by some minimum threshold. We then calculated the likelihood of counter-streaming occurring by dividing these counter-streaming events by the total number of events obtained in the same spatial bin. Bins with 20+ events, like the black bin in panel d, contained clusters of events with closely-spaced time stamps, which we found were associated with solar flare events. While solar disturbances produce outliers, they do not affect the overall trends.

The major trend is that the occurrence rate of counter streaming is non-uniform in the MSO frame. Figure 8 panel c shows a greater likelihood of observing counter streaming on the dusk side of the planet when the strongest crustal fields are near the dusk terminator compared to other orientations of the planet (panels b,d, or e). Further, there appears to be a dawn-dusk asymmetry. When looking at the duskward side of the planet, counter streaming is more likely when the crustal fields are near midnight (panel b) and the dusk terminator (panel c). Conversely, when looking dawnward, counter streaming is more likely when the crustal fields are near noon (panel h) and the dawn terminator (panel i). Figure 8 shows that the geometry of our case study (crustal fields near the dusk terminator) is favorable to observing counter streaming because panel c had twice the occurrence rate of all tested planetary orientations.

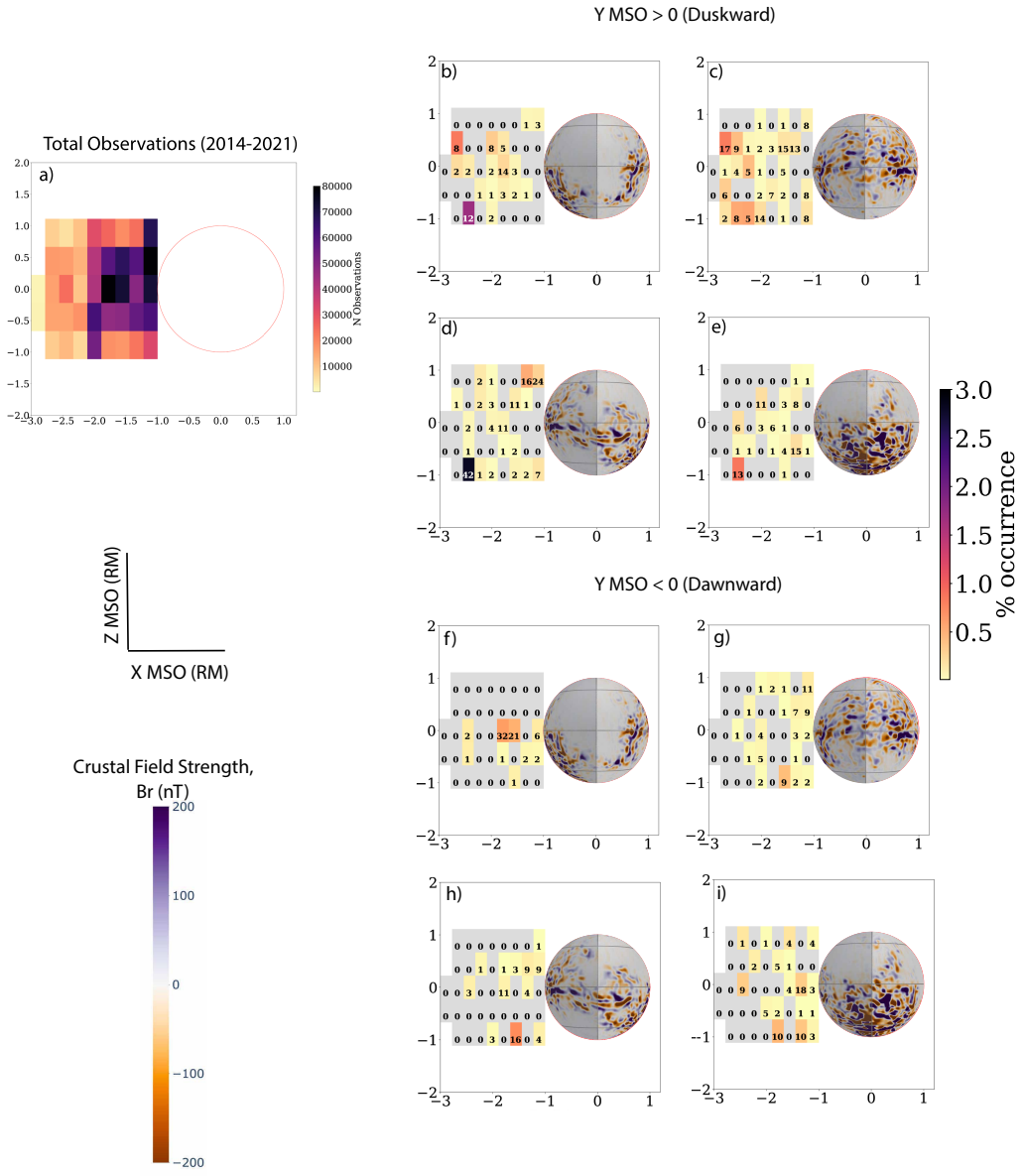

Figure 8. All MAVEN magnetotail observations ($\sqrt{Y_{MSO}^2 + Z_{MSO}^2} < 1R_M$ and $X_{MSO} < -1$) in the X-Z MSO plane between 2014-2021, with the colorscale representing number of observations (panel a). Panels b-e (f-i) show the duskward (dawnward) component of counter-streaming occurrence rates (colorbar on the middle-right side of the plot) for sub-solar longitudes of 0±45, 90±45, 180±45, and 270±45 degrees corresponding to the crustal fields located at midnight, the dusk terminator, noon, and the dawn terminator, respectively. In panels b-i, the number of counter-streaming events per bin is labeled in each respective bin, and the (Langlais et al., 2019) model is projected onto Mars. The color contours represent the direction of the magnetic field (radial inward/outward), as shown by the colorbar on the bottom left of the plot.

5 Discussion

We have analyzed MAVEN plasma and magnetic field measurements when the spacecraft was downstream of strong crustal magnetic sources located near the evening terminator. We observed multiple magnetic field rotations, and topological changes over spatial scales that are small in comparison to the dimensions of the magnetotail, as well as counter-streaming electrons from 1300 to 2000 km altitude. Taken together, these observations reveal a complex interaction between the draped IMF and crustal magnetic fields that produces a current system and potential structures extending into the magnetotail.

Multiple magnetic field rotations, most with associated amplitude drops, together with numerous topological changes suggest reconnection between the draped IMF and the crustal magnetic fields. C. F. Bowers et al. (2023) showed that repeated cycling between open/draped and closed topology acts as an indirect method for observing magnetic reconnection. The closed topology shown in Figure 6 a-c and Figure 7 (panel 1) could be explained by a crustal magnetic loop with both footpoints connected to the nightside ionosphere (e.g. Xu et al. (2017)). In this case, the 60-degree loss cones would correspond to a magnetic field amplitude of 30 nT at the footpoints (∼170 km altitude). Crustal fields of this strength are present upstream of the spacecraft, although at 3300 km altitude, we cannot determine the locations of the footpoints, if present. For solar wind electrons to become trapped onto the field lines, they either drifted across from draped fields, or were present before the field reconnected to form a loop at some earlier time. Given the small field gradients and large radii of field curvature of draped field lines in the magnetotail, drifting is unlikely. Reconnection can explain the observed energization through the reconnection process itself (e.g. Øieroset et al. (2002)) or by Fermi acceleration as the highly extended loop relaxes back to its equilibrium shape (e.g. Egedal et al. (2005); Drake et al. (2006)). An alternative explanation is that this trapping region is a detached flux rope (e.g. D. A. Brain et al. (2010); Hara et al. (2015)), possibly originating from a crustal source. In either case, the location of the trapping region downstream of crustal magnetic sources strongly suggests that they are formed by reconnection with those sources.

We find that other mechanisms, such as radial IMF conditions (eg. Masunaga et al. (2011)) and the magnetotail current sheet flapping (e.g. DiBraccio et al. (2017)), are less likely to explain the rapid magnetic field rotations and topological changes. First, radial IMF conditions are unlikely because the upstream IMF clock angle (measured 2.5 hours before and 2 hours after the observations presented here) was -140 deg and the IMF cone angle was +75 deg, typical of a Parker spiral configuration. Further, a recent case study by Fowler et al. (2022) showed that the magnetosphere became highly disturbed during radial IMF conditions, and similar disturbances were not observed for several orbits before, during, and after our case study. Second, sample current sheet crossings indicative of the tail current sheet flapping (DiBraccio et al., 2017) had larger timescales compared to those reported in this study. Assuming that the current regions are static structures, we found that the amount of time it took the spacecraft to cross current sheets in DiBraccio et al. (2017)'s study were at least a minute. In this study, the observed current region crossing timescales were shorter, at a few 10's of seconds. Therefore, we are confident that the magnetic field rotations reported in this study were not caused by the tail current sheet flapping or radial IMF conditions.

The fact that counter-streaming electrons are twice as likely to be observed when the crustal fields are located near the evening terminator compared to other planetary orientations suggests that this electron distribution is a feature of the solar wind interaction with the crustal fields. Figures 2 and 4 show that during counter streaming, the peak energy of the electron energy flux spectrum increases up to 120 eV. Note that these observations are rare, given an overall occurrence rate of 2.8%. This occurrence rate agrees with D. Brain et al. (2007)'s counter-streaming occurrence rate of 3% using MGS ob-

servations at 400 km altitude and 2 am local time. Our observations extend this low occurrence rate over a wide range of altitudes and local times in the tail.

A schematic that illustrates one possible explanation for our observations is presented in Figure 9. The crustal fields are on the dusk terminator, and when the IMF drapes about the planet, reconnection occurs. The newly reconnected field lines subsequently convect tailward, where their opposite polarities result in currents. Reconnection supports the observations of energized electrons (e.g. Dahlin (2020)), as well as the topological changes over relatively short timescales. Reconnection is associated with a variety of plasma phenomena, including the possibility that it might be associated with discrete aurora on Mars. The body of evidence in support of this hypothesis is growing (e.g. C. Bowers et al. (2023); Xu, Poppe, et al. (2019)). Our study adds to this evidence because we observe signatures associated with magnetic reconnection, and counter-streaming electrons, which are observed above active auroral arcs at Earth.

At Earth, electrons can become energized after open magnetic field lines reconnect in the tail to form an extended loop. The newly formed closed loop relaxes by moving towards the planet and possibly rotating, depending on the locations of the new footpoints. As the closed loop contracts, electrons undergo Fermi acceleration (e.g. Hoshino & Mukai (2002)). In addition, if the relaxation imposes currents, then double layers can form wherever the plasma cannot support the current. These double layers also accelerate electrons (e.g. Ergun et al. (2004)). Spacecraft such as Cluster and FAST measured these field-aligned potential structures, and a key signature in the plasma is counter-streaming, energized electrons (e.g. Imajo et al. (2022); Carlson et al. (1998); Hwang et al. (2013)). These field-aligned potential structures and the counter-streaming electrons associated with them are well constrained at Earth due to simultaneous measurements from multiple spacecraft (e.g. Klumpar et al. (1988)). While Mars does not yet have a dedicated auroral observatory, this case study presents indirect evidence towards the high-altitude field-aligned potential structure that gives rise to discrete aurora at Mars.

6 Conclusion

We have presented MAVEN plasma and magnetic field data obtained during an orbit in which the spacecraft passed through the tail downstream of strong crustal magnetic fields that were located near the evening terminator. The region of study contains complex magnetic field morphology, with multiple field rotations on spatial scales that are small compared with the overall dimensions of the tail. Magnetic field rotations and amplitude drops reveal the presence of currents. In addition, numerous topological changes between open, closed, and draped show that magnetic reconnection is an important mechanism for establishing this complex morphology. Because of the observing geometry, magnetic reconnection is likely between the draped IMF and the strong crustal magnetic fields. Electrons are energized by the reconnection process or by relaxation of recently closed magnetic loops to energies that could cause auroral emissions if the electrons precipitated into the atmosphere. Counter-streaming electrons, which are generally rare in the magnetotail, were observed between 1300 and 2000 km altitude in our study. From a statistical analysis, we showed that counter streaming is twice as likely to occur downsteam of strong crustal magnetic fields when they are located near the evening terminator. Thus, counter streaming is associated with the crustal fields and is likely a feature that occurs during such planetary orientations.

While the magnetotails of Mars and Earth are inherently different, the two systems share similarities (e.g. DiBraccio et al. (2018); Harada et al. (2017)). We present indirect evidence for a previously unexplored similarity: that of a field-aligned potential structure that gives rise to auroral emissions. Since counter-streaming electrons are associated with a field-aligned potential structure, and are the auroral precursors at Earth, we propose that the counter-streaming electrons observed here are also auroral precursors.

That precipitating particles can generate aurora is widely accepted; however, the processes involved in how the particles are accelerated are still outstanding. This study contributes to this active body of research and our future work will analyze the physics behind such processes.

Acknowledgments

The authors would like to thank the anonymous reviewers for their feedback. MN would like to thank A.R. Azari and D.A. Brain for their contributions to Figures 8 and 1 respectively. This work was funded by NASA's FINESST program (80NSSC21K1540), the Robert P. Lin Fellowship, and MAVEN mission funds. Data used in this study are available on the NASA Planetary Data System, via https://pds.nasa.gov/.

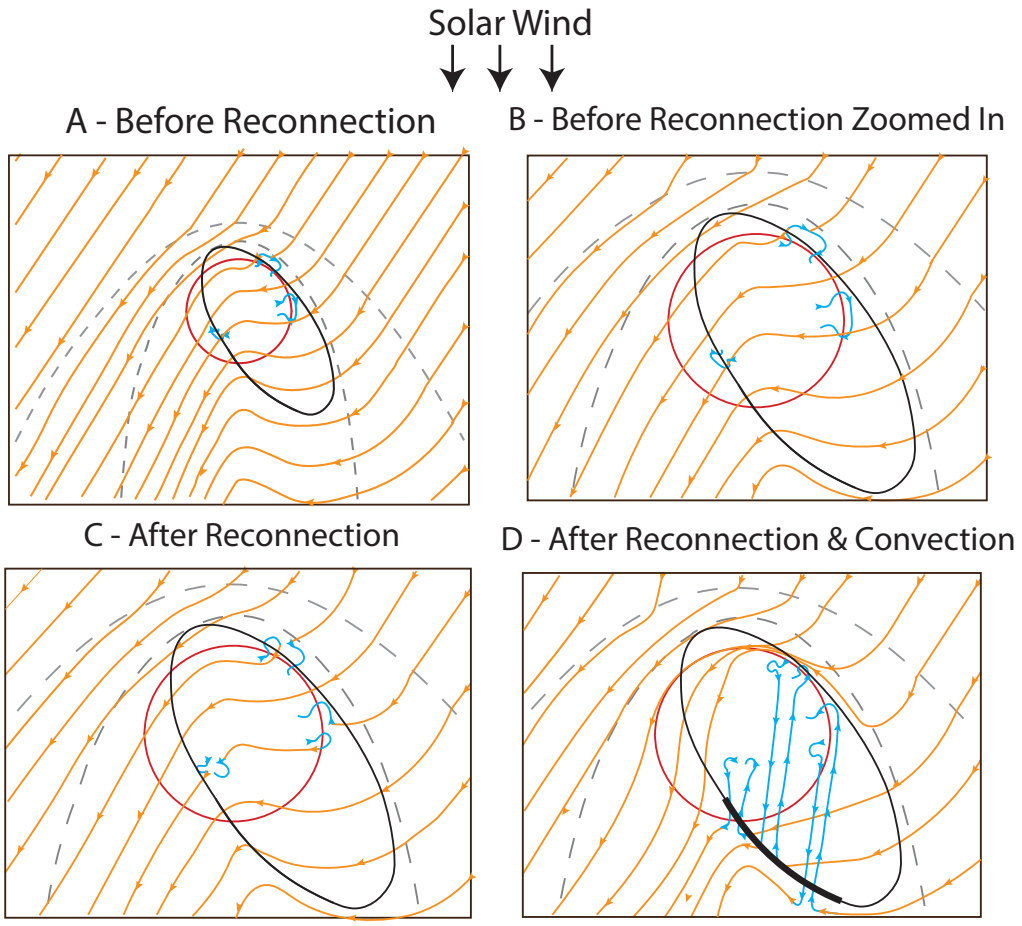

Figure 9. Schematic of the Martian system during the observations reported in this study in the MSO XY plane. The sun is at the top of the page and the planet's south pole is pointing out of the page. The solar wind IMF (orange lines) travels down the page and the IMF drapes about the planet. Panel A shows a overview of the system, with the crustal fields at the dusk terminator. Panel B shows a zoomed in perspective of panel A. Panel C shows the crustal fields (blue lines) reconnected with the IMF. Panel D shows the reconfigured fields after they have been convected down the magnetotail due to solar wind motion. The thick portion of black orbit in panel D is the spacecraft position during the times investigated in this study. MAVEN encounters multiple current regions created by the opposite magnetic polarity of the convected magnetic fields. Note that this cartoon is a 3D image onto a 2D plane, where we assume simultaneous reconnection is occurring at each site. In reality, the magnetic field lines would not cross.

References

Acuña, M. H., Connerney, J. E. P., Wasilewski, P., Lin, R. P., Anderson, K. A., Carlson, C. W., ... Ness, N. F. (1998). Magnetic field and plasma observations at mars: Initial results of the mars global surveyor mission. *Science*, *279*(5357), 1676-1680. doi: 10.1126/science.279.5357.1676

Bowers, C., DiBraccio, G., Slavin, J., Johnston, B., Schneider, N., Brain, D., & Azari, A. (2023). Evidence for magnetic reconnection as the precursor to discrete aurora at mars. *Journal of Geophysical Research: Space Physics*.

Bowers, C. F., DiBraccio, G. A., Slavin, J. A., Gruesbeck, J. R., Weber, T., Xu, S., ... Harada, Y. (2023). Exploring the solar wind-planetary interaction at mars: Implication for magnetic reconnection. *Journal of Geophysical Research: Space Physics*, *128*(2), e2022JA030989. doi: https://doi.org/10.1029/2022JA030989

Brain, D., Lillis, R., Mitchell, D., Halekas, J., & Lin, R. (2007). Electron pitch angle distributions as indicators of magnetic field topology near mars. *Journal of Geophysical Research: Space Physics*, *112*(A9).

Brain, D. A., Baker, A. H., Briggs, J., Eastwood, J. P., Halekas, J. S., & Phan, T.-D. (2010). Episodic detachment of martian crustal magnetic fields leading to bulk atmospheric plasma escape. *Geophysical Research Letters*, *37*(14). doi: https://doi.org/10.1029/2010GL043916

Carlson, C. W., McFadden, J. P., Ergun, R. E., Temerin, M., Peria, W., Mozer, F. S., ... Pfaff, R. (1998). Fast observations in the downward auroral current region: Energetic upgoing electron beams, parallel potential drops, and ion heating. *Geophysical Research Letters*, *25*(12), 2017-2020.

Connerney, J., Espley, J., Lawton, P., Murphy, S., Odom, J., Oliversen, R., & Sheppard, D. (2015). The maven magnetic field investigation. *Space Science Reviews*, *195*(1-4), 257–291.

Dahlin, J. T. (2020, 10). Prospectus on electron acceleration via magnetic reconnection. *Physics of Plasmas*, *27*(10), 100601. doi: 10.1063/5.0019338

DiBraccio, G. A., Dann, J., Espley, J. R., Gruesbeck, J. R., Soobiah, Y., Connerney, J. E. P., ... Jakosky, B. M. (2017). Maven observations of tail current sheet flapping at mars. *Journal of Geophysical Research: Space Physics*, *122*(4), 4308-4324. doi: https://doi.org/10.1002/2016JA023488

DiBraccio, G. A., Espley, J. R., Gruesbeck, J. R., Connerney, J. E., Brain, D. A., Halekas, J. S., ... others (2015). Magnetotail dynamics at mars: Initial maven observations. *Geophysical Research Letters*, *42*(21), 8828–8837.

DiBraccio, G. A., Luhmann, J. G., Curry, S. M., Espley, J. R., Xu, S., Mitchell, D. L., ... others (2018). The twisted configuration of the martian magnetotail: Maven observations. *Geophysical Research Letters*, *45*(10), 4559–4568.

Drake, J., Swisdak, M., Che, H., & Shay, M. (2006). Electron acceleration from contracting magnetic islands during reconnection. *Nature*, *443*(7111), 553–556.

Eastwood, J. P., Videira, J. J. H., Brain, D. A., & Halekas, J. S. (2012). A chain of magnetic flux ropes in the magnetotail of mars. *Geophysical Research Letters*, *39*(3). doi: https://doi.org/10.1029/2011GL050444

Egedal, J., Øieroset, M., Fox, W., & Lin, R. P. (2005, Jan). In situ discovery of an electrostatic potential, trapping electrons and mediating fast reconnection in the earth's magnetotail. *Phys. Rev. Lett.*, *94*, 025006. doi: 10.1103/PhysRevLett.94.025006

Ergun, R. E., Andersson, L., Main, D., Su, Y.-J., Newman, D. L., Goldman, M. V., ... Mozer, F. S. (2004). Auroral particle acceleration by strong double layers: The upward current region. *Journal of Geophysical Research: Space Physics*, *109*(A12). doi: https://doi.org/10.1029/2004JA010545

Fowler, C. M., Hanley, K. G., McFadden, J., Halekas, J., Schwartz, S. J., Mazelle, C., ... Curry, S. (2022). A maven case study of radial imf at mars: Impacts on

the dayside ionosphere. *Journal of Geophysical Research: Space Physics*, *127*(12), e2022JA030726. doi: https://doi.org/10.1029/2022JA030726

Gosling, J. T., Skoug, R. M., McComas, D. J., & Smith, C. W. (2005). Magnetic disconnection from the sun: Observations of a reconnection exhaust in the solar wind at the heliospheric current sheet. *Geophysical Research Letters*, *32*(5). doi: https://doi.org/10.1029/2005GL022406

Halekas, J., Eastwood, J., Brain, D., Phan, T., Øieroset, M., & Lin, R. (2009). In situ observations of reconnection hall magnetic fields at mars: Evidence for ion diffusion region encounters. *Journal of Geophysical Research: Space Physics*, *114*(A11).

Hara, T., Harada, Y., Mitchell, D. L., DiBraccio, G. A., Espley, J. R., Brain, D. A., ... others (2017). On the origins of magnetic flux ropes in near-mars magnetotail current sheets. *Geophysical Research Letters*, *44*(15), 7653–7662.

Hara, T., Mitchell, D. L., McFadden, J. P., Seki, K., Brain, D. A., Halekas, J. S., ... Jakosky, B. M. (2015). Estimation of the spatial structure of a detached magnetic flux rope at mars based on simultaneous maven plasma and magnetic field observations. *Geophysical Research Letters*, *42*(21), 8933-8941. doi: https://doi.org/10.1002/2015GL065720

Harada, Y., Halekas, J., McFadden, J., Mitchell, D., Mazelle, C., Connerney, J., ... others (2015). Magnetic reconnection in the near-mars magnetotail: Maven observations. *Geophysical Research Letters*, *42*(21), 8838–8845.

Harada, Y., Halekas, J. S., McFadden, J. P., Espley, J., DiBraccio, G. A., Mitchell, D. L., ... Jakosky, B. M. (2017). Survey of magnetic reconnection signatures in the martian magnetotail with maven. *Journal of Geophysical Research: Space Physics*, *122*(5), 5114-5131. doi: https://doi.org/10.1002/2017JA023952

Hoshino, M., & Mukai, T. (2002). Suprathermal electrons during magnetic reconnection: Fermi model. *Advances in Space Research*, *30*(7), 1639-1644. doi: https://doi.org/10.1016/S0273-1177(02)00428-3

Hwang, K.-J., Goldstein, M. L., Wendel, D. E., Fazakerley, A. N., & Gurgiolo, C. (2013). Cluster observations near reconnection x lines in earth's magnetotail current sheet. *Journal of Geophysical Research: Space Physics*, *118*(7), 4199-4209. doi: https://doi.org/10.1002/jgra.50403

Imajo, S., Miyoshi, Y., Asamura, K., Shinohara, I., Nosé, M., Shiokawa, K., ... Teramoto, M. (2022). Signatures of auroral potential structure extending through the near-equatorial inner magnetosphere. *Geophysical Research Letters*, *49*(10), e2022GL098105. (e2022GL098105 2022GL098105) doi: https://doi.org/10.1029/2022GL098105

Jakosky, B. M., Lin, R., Grebowsky, J., Luhmann, J., Mitchell, D., Beutelschies, G., ... others (2015). The mars atmosphere and volatile evolution (maven) mission. *Space Science Reviews*, *195*(1-4), 3–48.

Klumpar, D. M., Quinn, J. M., & Shelley, E. G. (1988). Counter-streaming electrons at the geomagnetic equator near 9 re. *Geophysical Research Letters*, *15*(11), 1295-1298. doi: https://doi.org/10.1029/GL015i011p01295

Langlais, B., Thébault, E., Houliez, A., Purucker, M. E., & Lillis, R. J. (2019). A new model of the crustal magnetic field of mars using mgs and maven. *Journal of Geophysical Research: Planets*, *124*(6), 1542-1569. doi: https://doi.org/10.1029/2018JE005854

Luhmann, J. G., Dong, C., Ma, Y., Curry, S. M., Mitchell, D., Espley, J., ... Mazelle, C. (2015). Implications of maven mars near-wake measurements and models. *Geophysical Research Letters*, *42*(21), 9087-9094. doi: https://doi.org/10.1002/2015GL066122

Masunaga, K., Futaana, Y., Yamauchi, M., Barabash, S., Zhang, T. L., Fedorov, A. O., ... Okano, S. (2011). O+ outflow channels around venus controlled by directions of the interplanetary magnetic field: Observations of high energy o+ ions

around the terminator. *Journal of Geophysical Research: Space Physics*, *116*(A9). doi: https://doi.org/10.1029/2011JA016705

McFadden, J., Kortmann, O., Curtis, D., Dalton, G., Johnson, G., Abiad, R., ... others (2015). Maven suprathermal and thermal ion compostion (static) instrument. *Space Science Reviews*, *195*(1), 199–256.

Mitchell, D., Mazelle, C., Sauvaud, J.-A., Thocaven, J.-J., Rouzaud, J., Fedorov, A., ... others (2016). The maven solar wind electron analyzer. *Space Science Reviews*, *200*(1-4), 495–528.

Nauth, M., Fowler, C. M., Andersson, L., DiBraccio, G. A., Xu, S., Weber, T., & Mitchell, D. (2021). The influence of magnetic field topology and orientation on the distribution of thermal electrons in the martian magnetotail. *Journal of Geophysical Research: Space Physics*, *126*(3), e2020JA028130. doi: https://doi.org/10.1029/2020JA028130

Øieroset, M., Lin, R. P., Phan, T. D., Larson, D. E., & Bale, S. D. (2002, Oct). Evidence for electron acceleration up to ∼300ev in the magnetic reconnection diffusion region of earth's magnetotail. *Phys. Rev. Lett.*, *89*, 195001. doi: 10.1103/PhysRevLett.89.195001

Romanelli, N., Modolo, R., Leblanc, F., Chaufray, J.-Y., Hess, S., Brain, D., ... Jakosky, B. (2018). Effects of the crustal magnetic fields and changes in the imf orientation on the magnetosphere of mars: Maven observations and lathys results. *Journal of Geophysical Research: Space Physics*, *123*(7), 5315-5333.

Schneider, N. M., Milby, Z., Jain, S. K., Gérard, J.-C., Soret, L., Brain, D. A., ... Jakosky, B. M. (2021). Discrete aurora on mars: Insights into their distribution and activity from maven/iuvs observations. *Journal of Geophysical Research: Space Physics*, *126*(10), e2021JA029428. doi: https://doi.org/10.1029/2021JA029428

Vaisberg, O., & Smirnov, V. (1986). The martian magnetotail. *Advances in space research*, *6*(1), 301–314. doi: 10.1016/0273-1177(86)90046-3

Weber, T., Brain, D., Mitchell, D., Xu, S., Connerney, J., & Halekas, J. (2017). Characterization of low-altitude nightside martian magnetic topology using electron pitch angle distributions. *Journal of Geophysical Research: Space Physics*, *122*(10), 9777–9789.

Weber, T., Brain, D., Xu, S., Mitchell, D., Espley, J., Halekas, J., ... Jakosky, B. (2020). The influence of interplanetary magnetic field direction on martian crustal magnetic field topology. *Geophysical Research Letters*, *47*(19), e2020GL087757. doi: https://doi.org/10.1029/2020GL087757

Xu, S., Mitchell, D., Luhmann, J., Ma, Y., Fang, X., Harada, Y., ... DiBraccio, G. A. (2017). High-altitude closed magnetic loops at mars observed by maven. *Geophysical Research Letters*, *44*(22), 11,229-11,238. doi: https://doi.org/10.1002/2017GL075831

Xu, S., Poppe, A. R., Halekas, J. S., Mitchell, D. L., McFadden, J. P., & Harada, Y. (2019). Mapping the lunar wake potential structure with artemis data. *Journal of Geophysical Research: Space Physics*, *124*(5), 3360-3377. doi: https://doi.org/10.1029/2019JA026536

Xu, S., Weber, T., Mitchell, D. L., Brain, D. A., Mazelle, C., DiBraccio, G. A., & Espley, J. (2019). A technique to infer magnetic topology at mars and its application to the terminator region. *Journal of Geophysical Research: Space Physics*, *124*(3), 1823-1842. doi: https://doi.org/10.1029/2018JA026366

Yeroshenko, Y., Riedler, W., Schwingenschuh, K., Luhmann, J. G., Ong, M., & Russell, C. T. (1990). The magnetotail of mars: Phobos observations. *Geophysical Research Letters*, *17*(6), 885-888. doi: https://doi.org/10.1029/GL017i006p00885

Figure 4.

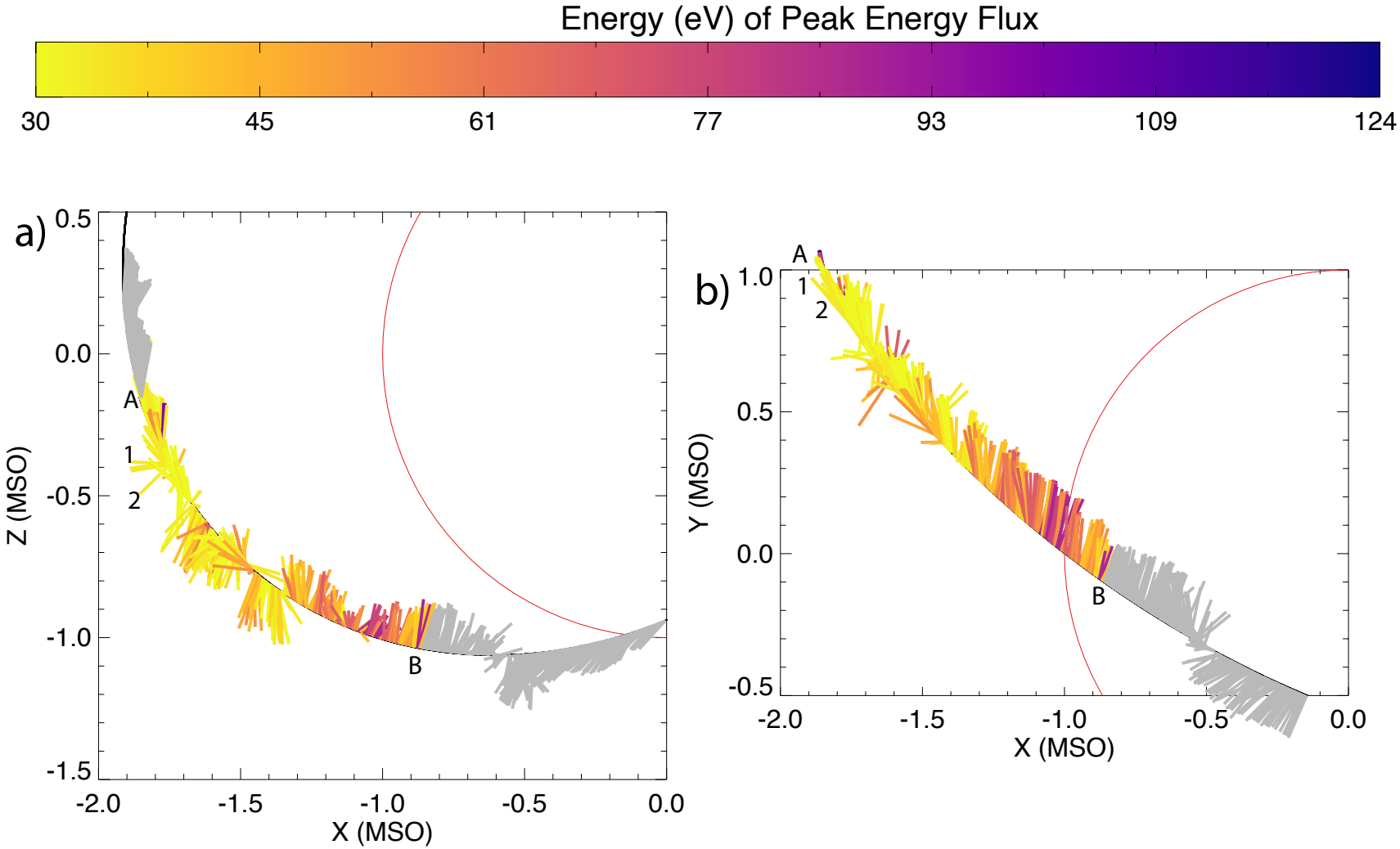
Energy (eV) of Peak Energy Flux
30
45
61
77
93
109
124
a)
Z (MSO)
X (MSO)
A
1
2
B
b)
Y (MSO)
X (MSO)
A
1
2
B

Figure 5.

a) M>12 amu Energy (eV)

b) M<10 amu Energy (eV)

c) H^+ Velocity (kms)

d) O^+ Velocity (kms)

e) O_2^+ Velocity (kms)

Z

Y [MSO]

X

alt 4126.5 3532.5 2857.2 2114.6 1342.8 637.2 196.0

hhmm 0830 0840 0850 0900 0910 0920 0930

2017 Dec 11

MAVEN c6 32e64m counts
2017-12-11/08:42:35-08:44:43

MAVEN c6 32e64m counts
2017-12-11/08:47:23-08:48:55

MAVEN c6 32e64m counts
2017-12-11/08:55:15-08:56:15

MAVEN c6 32e64m counts
2017-12-11/09:07:35-09:09:23

1) 2) 3) 4)

Mass/q (amu/q)

Energy/q (eV/q)

Log_{10}(counts)

Figure 6.

Trapped: 2017-12-11/08:42:55 - 08:43:15

a)

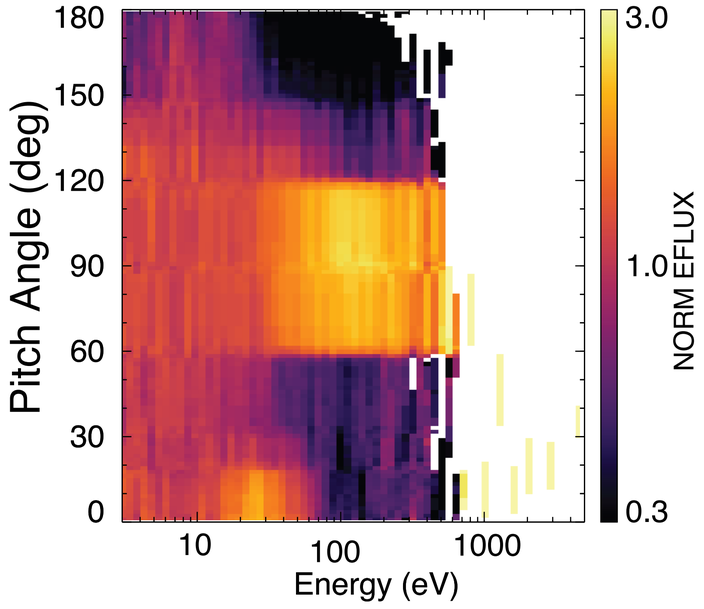

b)

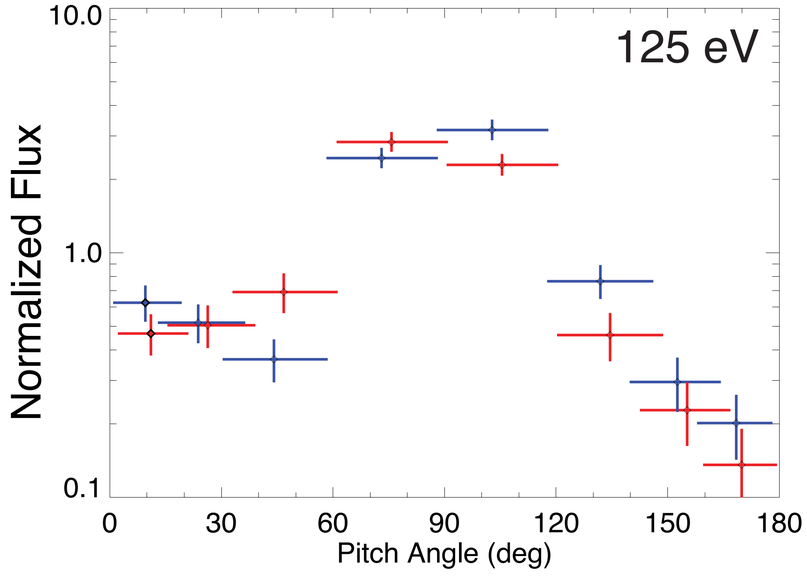

c)

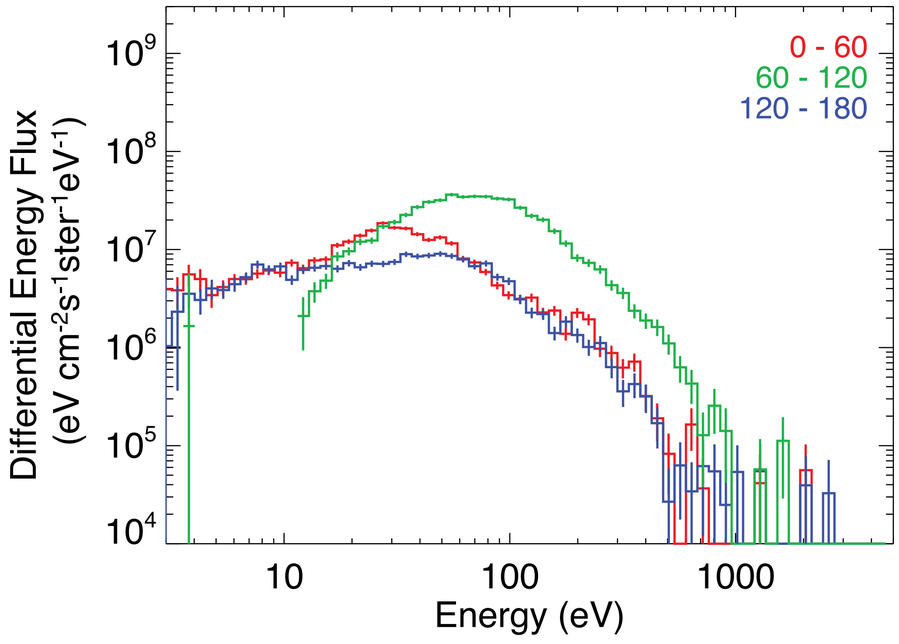

Counter-streaming 2017-12-11/09:02:15 - 09:02:25

d)

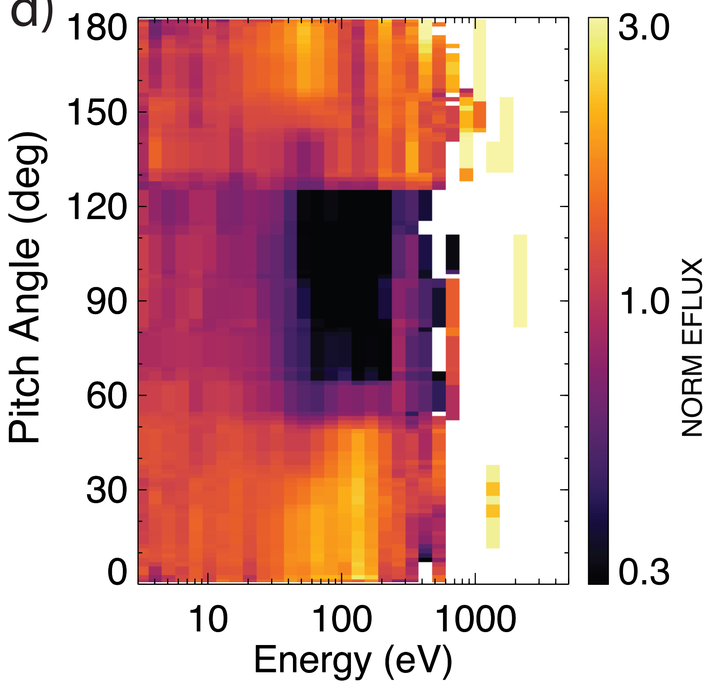

e)

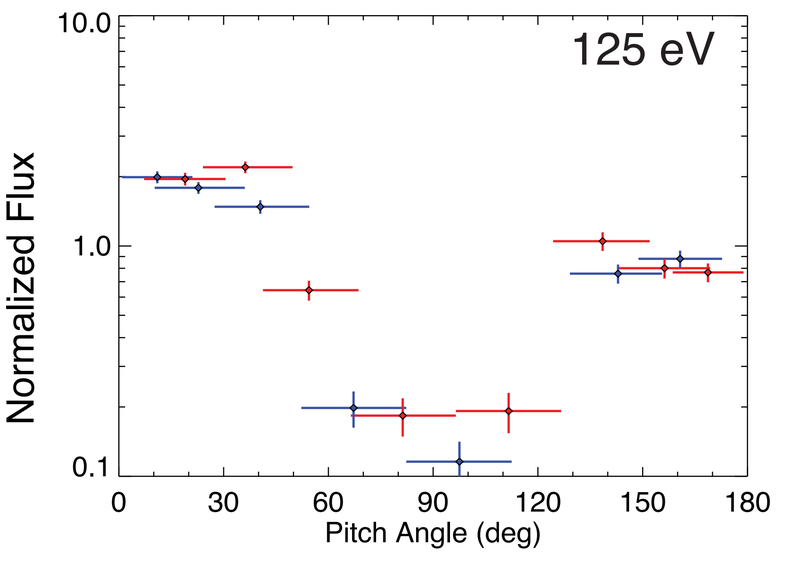

f)

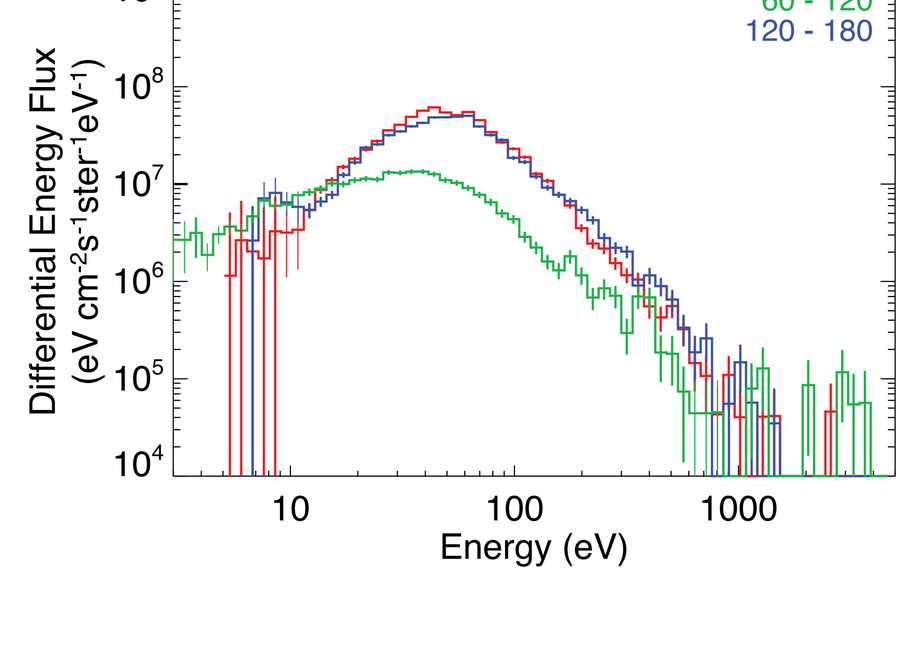

Figure 1.

a)

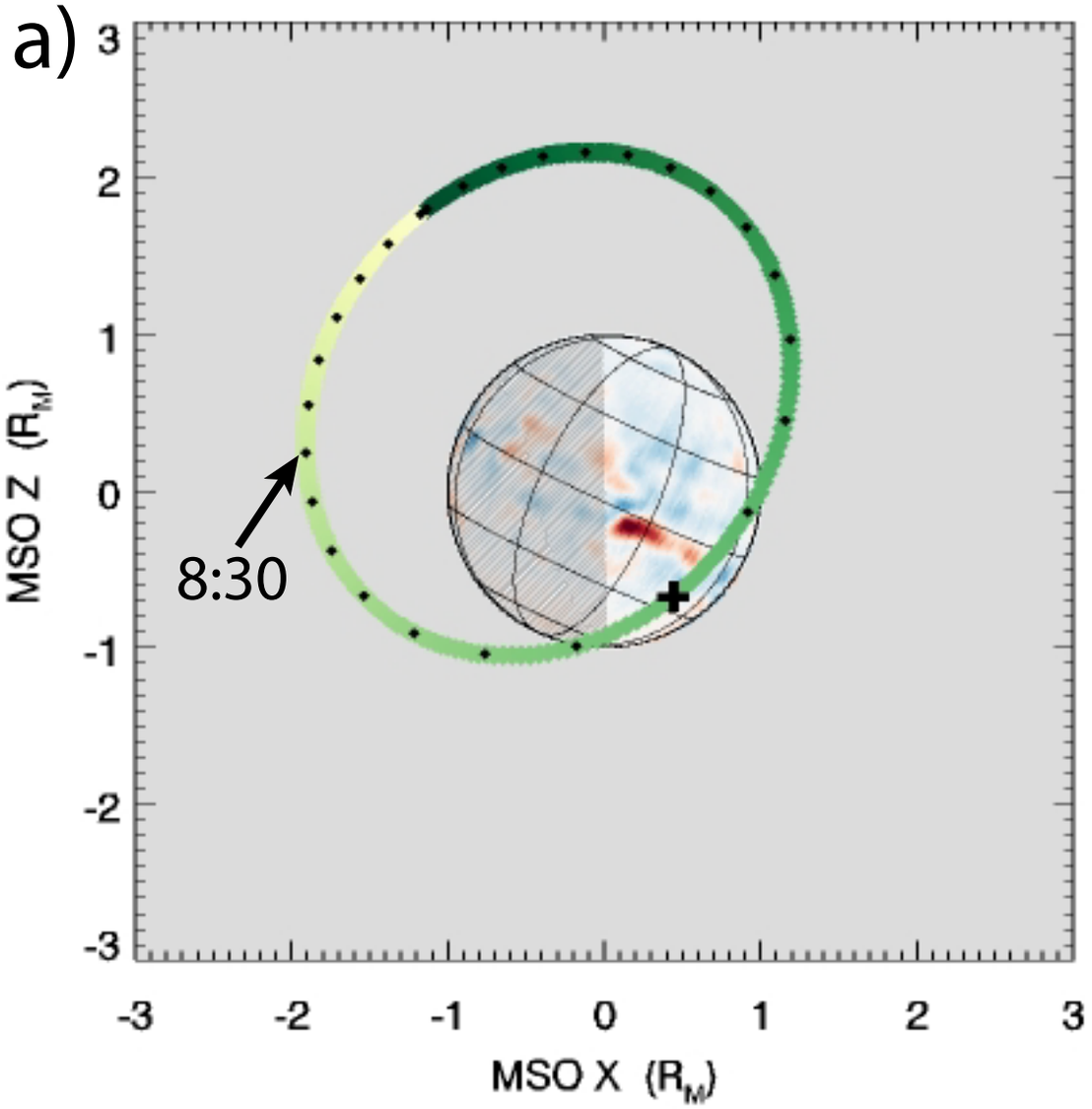
3
2
1
0
-1
-2
-3
MSO Z (R_M)
8:30
-3
-2
-1
0
1
2
3
MSO X (R_M)

b)

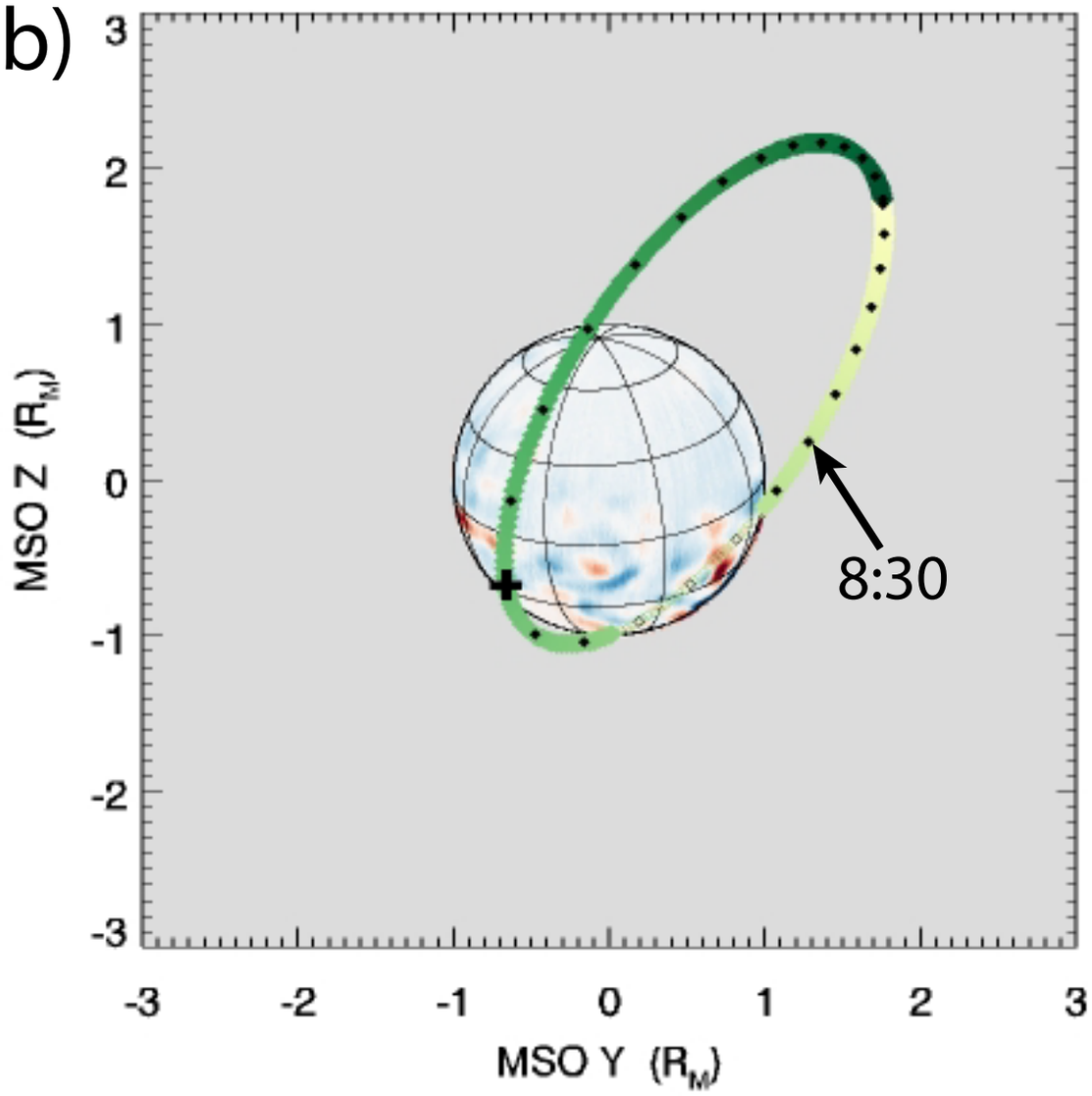
3
2
1
0
-1
-2
-3
MSO Z (R_M)
8:30
-3
-2
-1
0
1
2
3
MSO Y (R_M)

c)

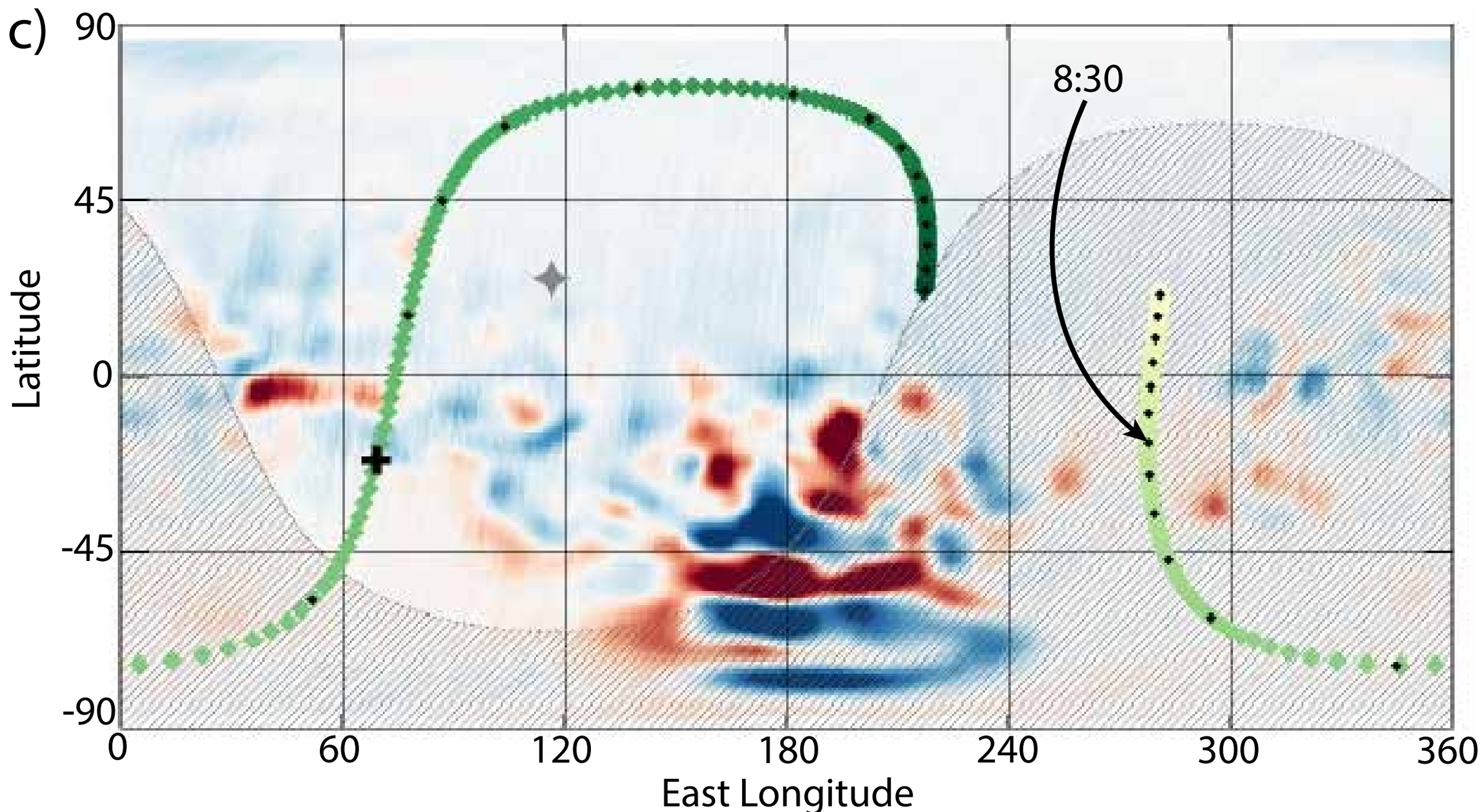
90
45
0
-45
-90
Latitude
8:30
0
60
120
180
240
300
360
East Longitude

Figure 7.

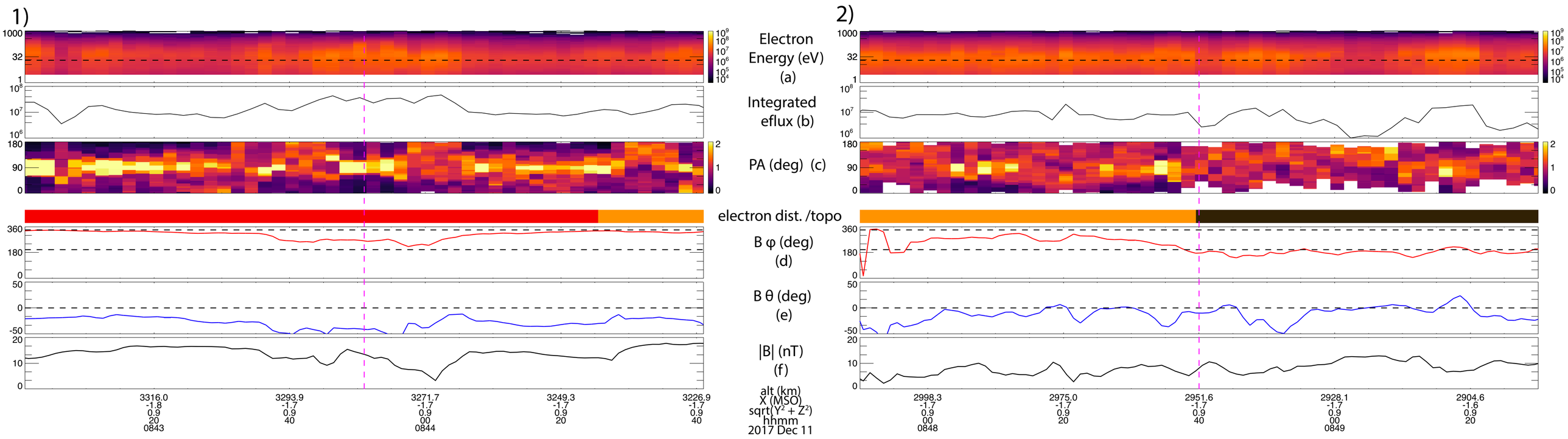
1)
2)
Electron Energy (eV) (a)
Integrated eflux (b)
PA (deg) (c)
electron dist. /topo
B φ (deg) (d)
B θ (deg) (e)
|B| (nT) (f)
alt (km)
X (MSO)
sqrt(Y² + Z²)
hhmm
2017 Dec 11
3316.0 -1.8 0.9 20 0843
3293.9 -1.7 0.9 40
3271.7 -1.7 0.9 00 0844
3249.3 -1.7 0.9 20
3226.9 -1.7 0.9 40
2998.3 -1.7 0.9 00 0848
2975.0 -1.7 0.9 20
2951.6 -1.7 0.9 40
2928.1 -1.7 0.9 00 0849
2904.6 -1.6 0.9 20

Figure 8.

Y MSO > 0 (Duskward)

Total Observations (2014-2021)

a)

b)

c)

d)

e)

Y MSO < 0 (Dawnward)

f)

g)

h)

i)

N Observations

% occurrence

Z MSO (RM)

X MSO (RM)

Crustal Field Strength,
Br (nT)

Figure 3.

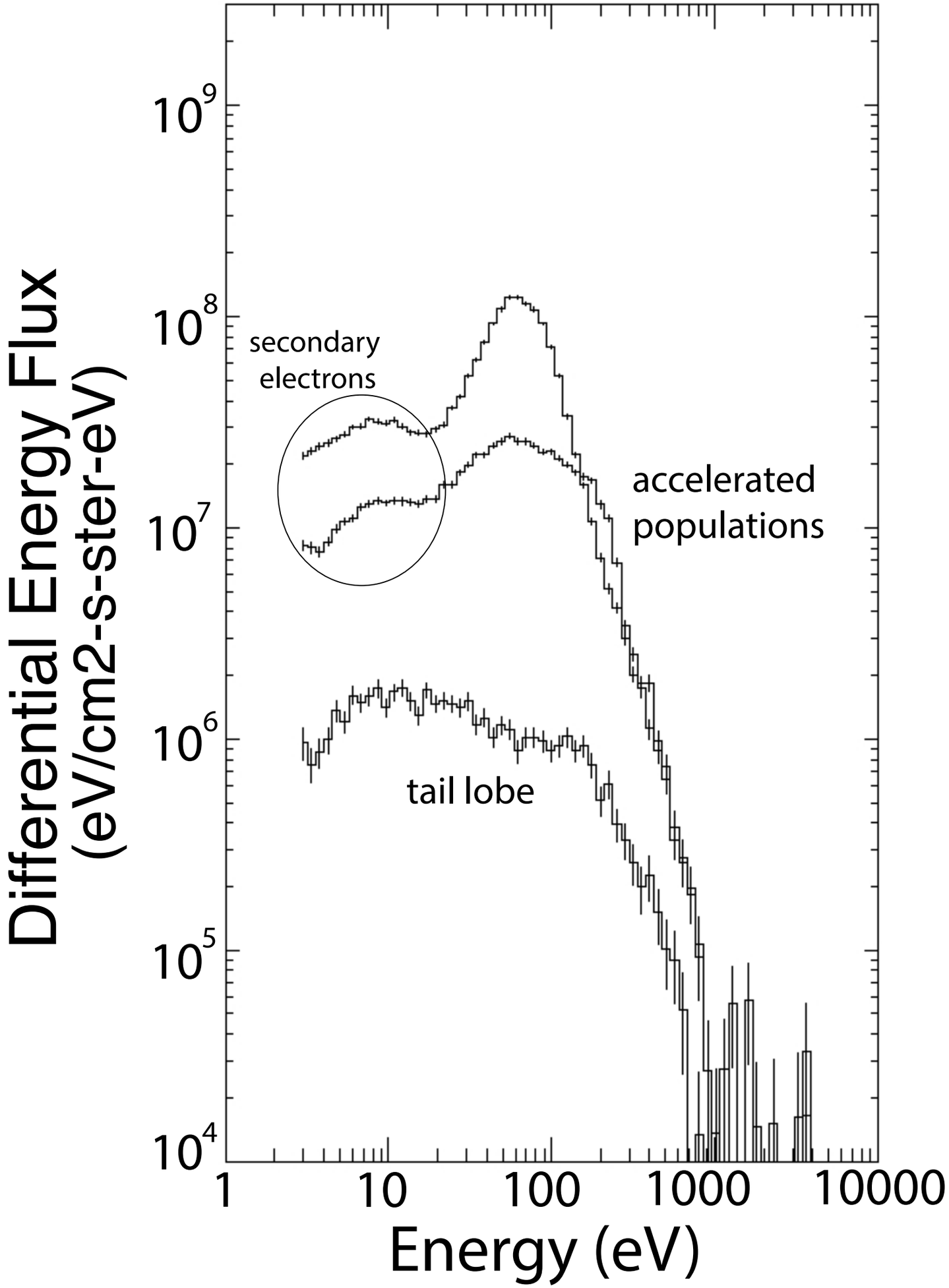
Differential Energy Flux
(eV/cm2-s-ster-eV)
10^9
10^8
10^7
10^6
10^5
10^4
secondary
electrons
accelerated
populations
tail lobe
1
10
100
1000
10000
Energy (eV)

Figure 9.

Solar Wind

A - Before Reconnection

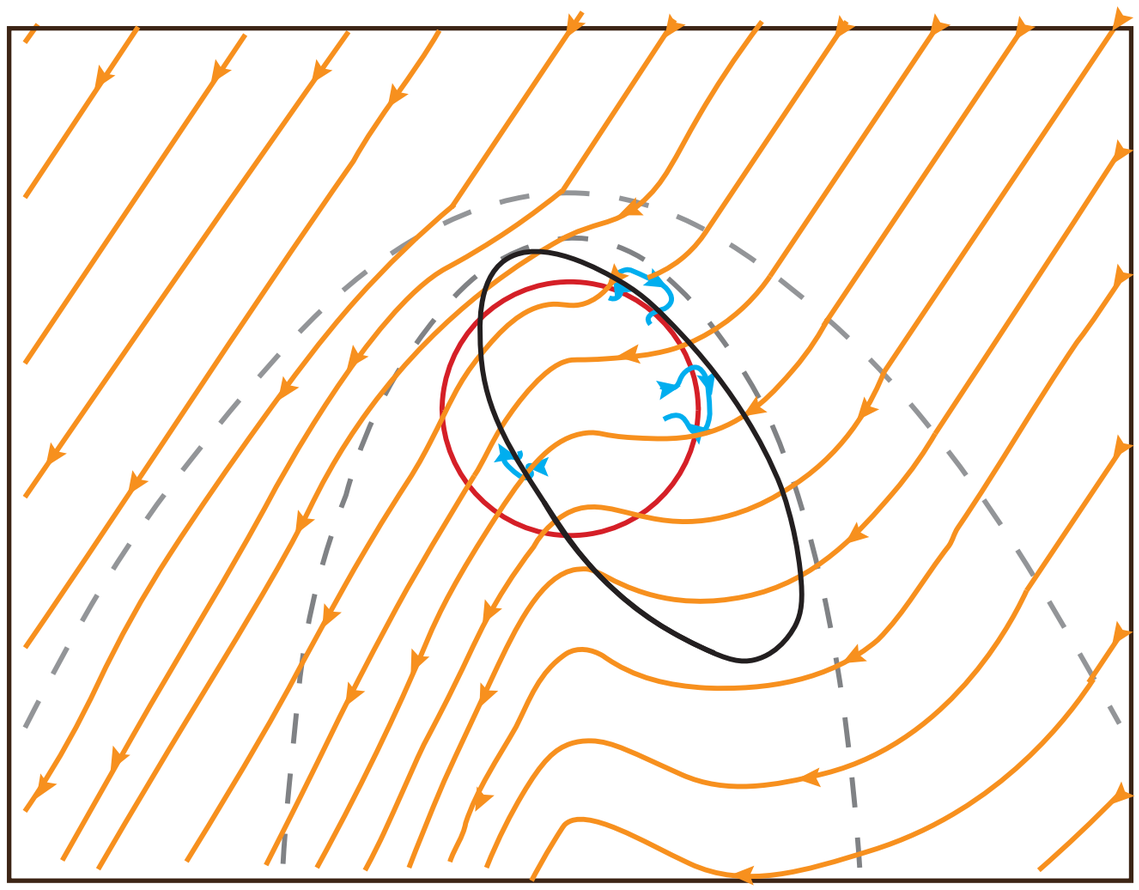

B - Before Reconnection Zoomed In

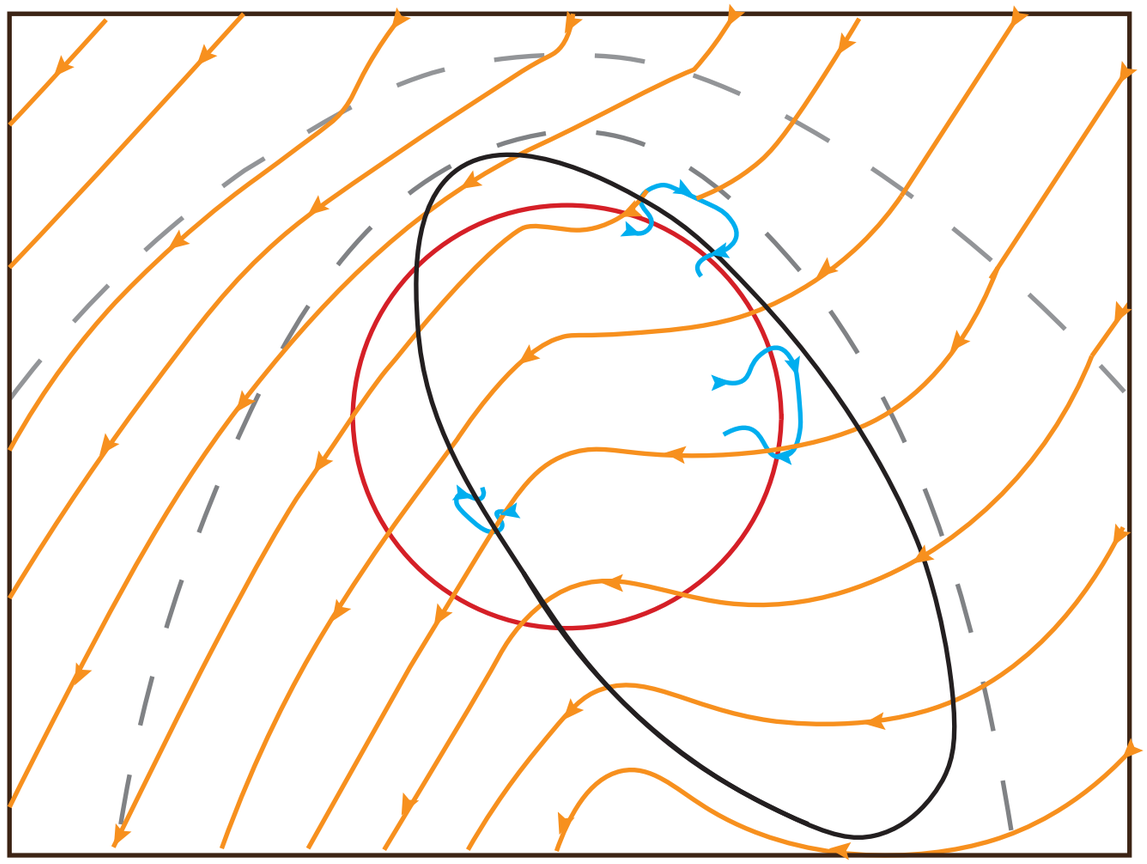

C - After Reconnection

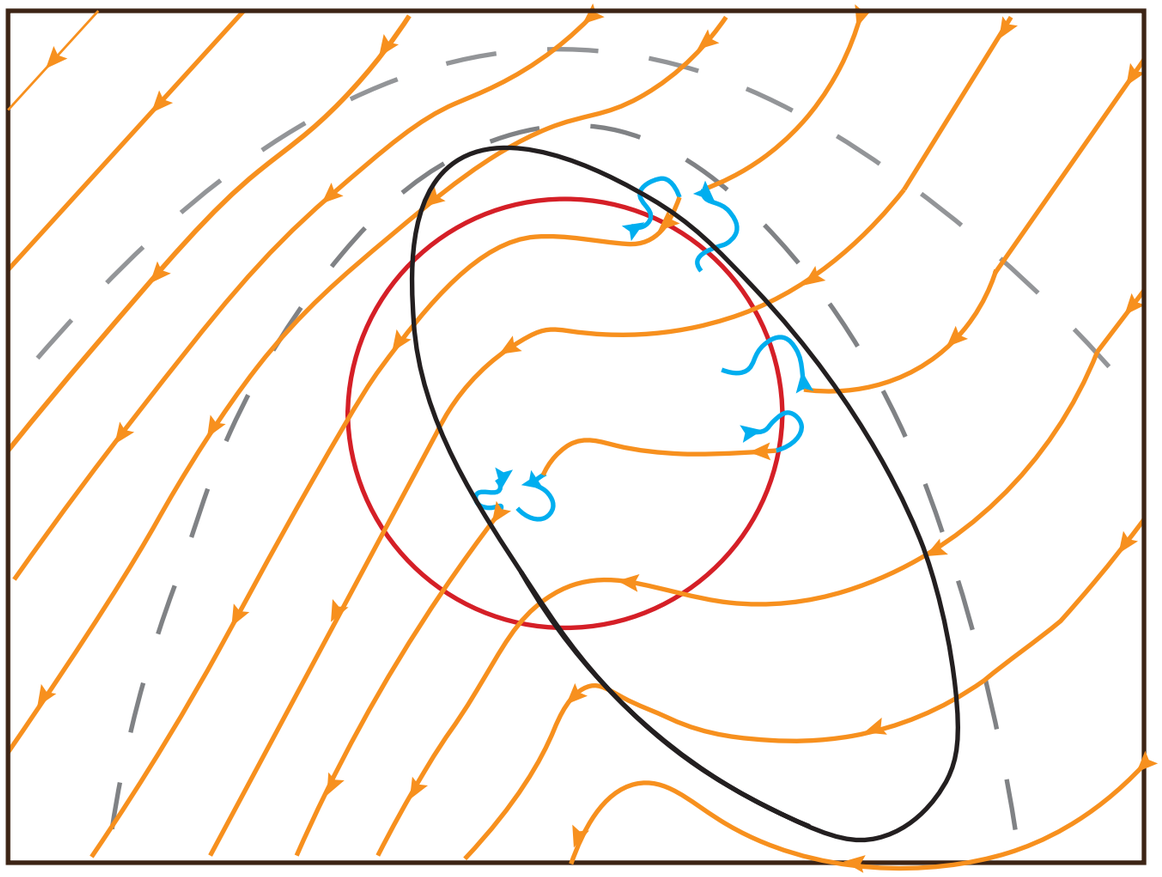

D - After Reconnection & Convection

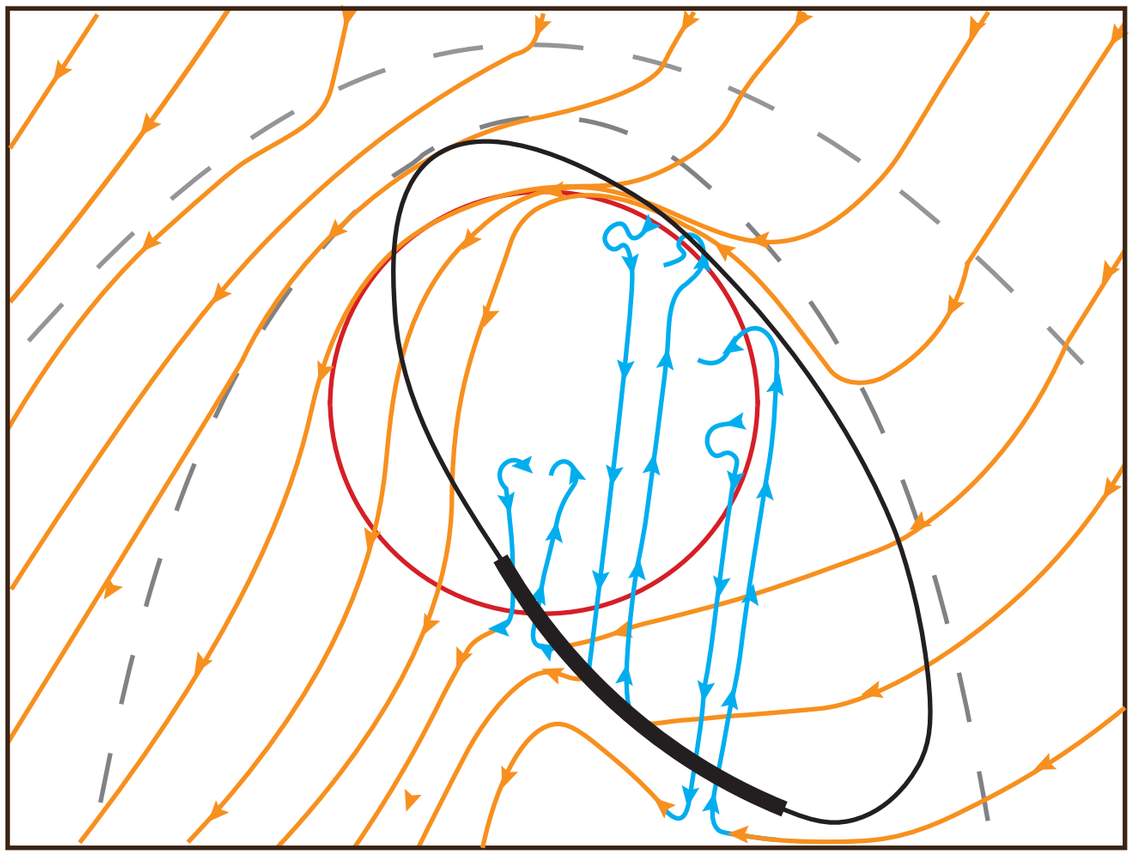

Figure 2.

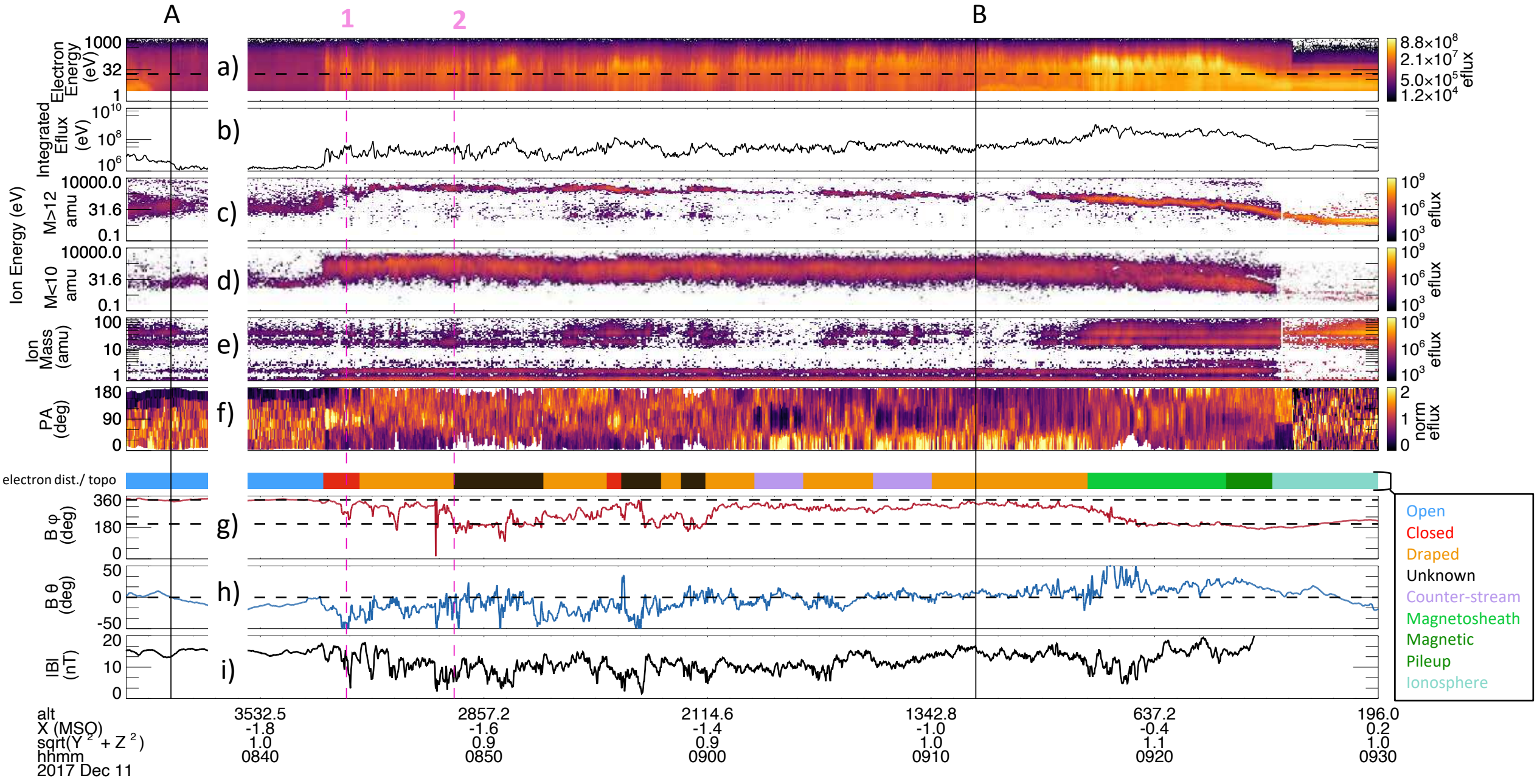
A
1
2
B
Electron Energy (eV)
1000
32
1
a)
8.8×10^8
2.1×10^7
5.0×10^5
1.2×10^4
eflux
Integrated Eflux (eV)
10^10
10^8
10^6
b)
Ion Energy (eV)
M>12 amu
10000.0
31.6
0.1
c)
10^9
10^6
10^3
eflux
M<10 amu
10000.0
31.6
0.1
d)
10^9
10^6
10^3
eflux
Ion Mass (amu)
100
10
1
e)
10^9
10^6
10^3
eflux
PA (deg)
180
90
0
f)
2
1
0
norm eflux
electron dist./ topo
B φ (deg)
360
180
0
g)
B θ (deg)
50
0
-50
h)
|B| (nT)
20
10
0
i)
Open
Closed
Draped
Unknown
Counter-stream
Magnetosheath
Magnetic
Pileup
Ionosphere
alt
X (MSO)
sqrt(Y 2 + Z 2)
hhmm
2017 Dec 11
3532.5
-1.8
1.0
0840
2857.2
-1.6
0.9
0850
2114.6
-1.4
0.9
0900
1342.8
-1.0
1.0
0910
637.2
-0.4
1.1
0920
196.0
0.2
1.0
0930